ELASTICITY AND BIOACTIVITY OF POROUS SILICON FILMS

JORDAN PECKHAM

Elasticity and Bioactivity of Porous Silicon Films

by

Jordan Peckham

A thesis submitted to the

School of Graduate Studies

in partial fulfillment of the

requirements for the degree of

Master of Science

Department of Physics

Memorial University of Newfoundland

August 18, 2011

St. John's Newfoundland

Abstract

Porous silicon films with a variety of porosities, pore geometries, and pore network morphologies were formed by electrochemical anodization of crystalline silicon in hydrofluoric acid-based electrolytes. The elastic properties of microporous films formed on p^- type substrates and mesoporous films formed on n^+ type substrates were characterized using Brillouin light scattering spectroscopy. Bioactivity of micro, meso, and macroporous silicon was assessed by monitoring the mass of samples over time while immersed in a simulated body fluid with a chemical composition that mimics that of human blood plasma. Scanning electron microscopy and energy dispersive x-ray studies reveal the presence of the bone-like mineral hydroxyapatite on some of the simulated body fluid-treated samples. Collectively, these studies provide a foundation for the use of porous silicon as a bioactive and elastically-adjustable bone-building matrix.

Contents

List of Tables

List of Figures

Chapter 1

Introduction

The next generation of biomaterials and tissue engineering will employ materials which facilitate self-healing with gradual depletion of the scaffold material *in vivo*, along with a tunable pore structure and elastic moduli [1]. Amongst the numerous natural and synthetic materials used, most tissue engineering scaffolds are porous and hence limited in use as orthopaedic scaffolds due to inadequate mechanical properties, lack of uniformity with regards to porosity, and a lack of osteoinductive ability [2]. In contrast, porous silicon structures have been shown to allow fast deposition of the bone-building material, hydroxyapatite, with strong bonds to the surface, as well as to induce rapid formation of physiologically stable hydroxyapatite when immersed in artificial body liquids or real body liquids [3, 4]. Also, porous silicon films of uniform porosity are easily produced, with tunable elastic moduli based on the resultant pore morphology and porosity. Knowledge of the mechanical properties allows designers

to accurately design and optimize structures based on these properties [5, 6].

A limited number of reports on the mechanical properties of porous silicon films are available since much of the research and application has been focused around electrical and optical properties of the material [5]. Detailed knowledge of the mechanical properties is of fundamental importance for materials in which rigidity and strength are crucial.

In this work, porous silicon films formed on p^-, p^+, and n^+ type bulk silicon with a broad range of porosities, pore morphologies, and pore geometries are reported. The mechanical properties and bioactivity of these porous silicon samples is presented.

1.1 Porous Silicon

Porous silicon (π-Si) formation occurs during electrochemical dissolution of crystalline silicon (c-Si) in hydrofluoric acid (HF) based electrolytes [7]. In 1956 the first report of the fabrication of porous silicon was published when studies of electrolytic shaping yielded black, brown, or red deposits, at the time assumed to be a suboxide of silicon [8,9]. An increase in the number of publications on porous silicon occurred in the early 1970's after the first model of pore formation on n-type silicon was proposed based on the breakdown of the depletion layer [10]. However, it was not until the 1990's that interest in porous silicon climaxed when the observation of visible photoluminescence at room temperature was reported [11].

The properties of porous silicon (porosity, pore geometry and morphology, film

thickness) depend directly on the anodization conditions, such as electrolyte and etching current density as well as parent wafer properties such as resistivity and dopant type. Understanding the dependence of porous silicon properties, such as the elastic moduli and the porosity on these conditions allows control of the fabrication such that the material can be tailored for specific applications [12].

Porosity refers to the volumetric fraction of crystalline silicon removed during etching. It is more generally defined as the ratio of the empty pore volume to the total volume [13]. Control of the resulting porosity in porous silicon films has further extended fabrication from single layer films to multilayered films in which the individual layers have alternatively high and low refractive index [14–16], and graded layers where the index of refraction steps to a higher or lower refractive index value [17, 18]. The porosity however does not provide any morphological information about the resultant film. In fact, porous silicon films with similar porosity values can be obtained in samples with different pore sizes, ranging from about 1 nm - 10 μm, and morphologies from sponge-like to perfect-cylindrical [19]. Information about the resulting structure and morphology is less often reported, possibly due to the challenges in determining this information and the fact that no complete understanding of the mechanisms leading to a particular morphology exists [12]. Instead, general results have been collected based on the large body of work on porous silicon with respect to the fabrication variables. These generally accepted characteristics based on parent wafer type are summarized in Table 1.1. Resultant porous silicon films are also

Table 1.1: General morphology of porous silicon samples based on parent wafer type.

Type	Resistivity	Pore Size	Pore Morphology
p^+	$< 0.05\ \Omega$·cm	10 - 100 nm	anisotropic with long, ordered voids perpendicular to the surface.
p^-	$> 0.2\ \Omega$·cm	1 - 5 nm,	homogeneous and interconnected network.
		$>1\ \mu$m	random and columnar pores.
n^+	$< 0.02\ \Omega$·cm	100 nm -1 μm	similar to p^+ with random filamentary net.
n^-	$> 0.02\ \Omega$·cm	10 nm - 1 μm	Filamentary net.

divided into three categories based on average pore size (by IUPAC standards) [20]:

- Microporous silicon: < 2 nm
- Mesoporous silicon: 2 - 50 nm
- Macroporous silicon: > 50 nm.

For samples made from p^+ type and n^+ type crystalline silicon, a systematic study on the pore size distribution using nitrogen adsorption experiments by Herino demonstrated a columnar and side-branched pore structure [21]. Further, for p^+ type samples it was found that an increase in current not only increased the porosity, but also increased the pore radius. A similar trend was noted when decreasing the HF concentration in the electrolyte. In the case of n^+ type porous silicon, the pore radius was found to increase with increasing sample thickness, which was attributed to the chemical dissolution of the porous layer as it was only notable for films $> 10\ \mu$m thick [21]. This trend has also been noted in thick p^+ and p^- type samples [22].

For p^- type samples the majority of the determined pore sizes have been shown to fall in the range of 1 - 5 nm [21,22]. Unlike p^+ type and n^+ type porous silicon however, it has been reported for p^- type porous silicon films that the applied current has little effect on the porosity [18, 23]. For n^- type samples, formation in the dark resulted in porosities below 10% with micron-size pores, while the addition of illumination during the fabrication resulted in much higher porosities with much smaller pores in the mesoporous regime [21].

The formation of macroporous silicon, with pores on the scale of $\sim 1\ \mu$m, formed on both n-type and p-type bulk silicon has been well documented by means of front side or back side illumination for n-type, and with no illumination for p-type in both aqueous and organic electrolytes [19]. The first report of the formation of macroporous silicon on p^- type substrates can be found in Ref. [24]. In the period since this report, macroporous silicon has been proposed and optimized for use in solar cells [25, 26], and has also been shown to promote maximum osteoblast cell growth and viability when compared to micro- and mesoporous silicon [27].

1.2 Mechanical Properties of Porous Silicon

The elastic properties of porous silicon films have been determined using several methods. Barla *et al.* determined the elastic constants of porous silicon films using X-ray diffraction, demonstrating behavior of a near perfect crystal and noting a difference between the values of Young's modulus of porous silicon and crystalline silicon [28].

Populaire *et al.* used topographic measurements and finite element simulations to determine the Young's modulus of p^+ type patterned porous silicon layers yielding values two orders of magnitude smaller than that of bulk silicon [29]. They also noted a large anisotropy in the Young's Modulus, calculated from the ratio of the parallel to the perpendicular component, which should be accounted for in further experiments and theoretical calculations. Da Fonseca *et al.* demonstrated a dependence of surface acoustic wave velocity, bulk acoustic wave velocity, and Young's modulus on the porosity for p^+ type samples using microechography and acoustic signature [30]. It was noted, based on empirical equations relating the porosity to the elastic properties, that the resulting porous film was relatively ordered.

Nanoindentation techniques have been used to determine Young's modulus of porous silicon films [5, 6, 31, 32]. Bellet *et al.* determined the Young's modulus of both p^+ and p^- type porous silicon, concluding that Young's modulus is strongly dependent on the doping level of c-Si and on the porosity. The Young's modulus value of a p^- type sample was shown to be five times smaller than that of a p^+ type sample of the same porosity [31]. Duttagupta *et al.* confirmed the results of Bellet through determination of microhardness [6]. Oisten *et al.* compared the Young's modulus of p^+ and n^+ type porous silicon samples, reporting a higher Young's modulus for p^+ type samples formed at the same current density. This result was attributed to differences in the resulting porosity and morphology of the p^+ and n^+ type samples formed at the same current density [5]. Further, in Ref. [32] using nanoindentation

techniques it is demonstrated that thermal oxidation of porous silicon films improved the mechanical properties (microhardness and Young's modulus) by approximately 30% compared to the as-prepared p^+ type porous silicon samples. It was also noted that in comparison to the as-prepared samples, an increase in the thermal oxidation temperature increased the Young's modulus and microhardness [32].

Determination of the elastic properties of porous silicon films by measuring the surface and bulk phonon velocities using Brillouin light scattering has also been reported. In Ref. [33], Brillouin light scattering was used to determine the phonon velocities in n^+ and p^- type samples of different porosity and morphology. Beghi reported in-depth inhomogeneities in both sample types, as well multiple surface modes in p-type samples, attributed to guided acoustic modes in the softened surface layer. Lockwood *et al.* obtained Brillouin spectra for p^- type π-Si revealing two acoustic phonon peaks associated with the surface and film modes of the porous layer [34].

A comprehensive Brillouin study by Fan *et al.* allowed identification of three types of acoustic modes in p^+ and p^- type silicon [23]. They noted an increased bulk phonon velocity for films less than 10 μm thick compared to films of the same porosity, explaining this result to be due to the presence of a transition layer between the porous layer and the substrate. Fan *et al.* also calculated the elastic constants and Young's modulus, demonstrating a non-linear relationship between these properties and the porosity, where the Young's Modulus, E, was related to the porosity, ξ as $E = 155(1-\xi)^{2.93}$ [23]. Reduction of the acoustic mode frequency shift for p^- type

films due to natural oxidation in ambient air has also been demonstrated. Fan *et al.* concluded that the change in frequency shift was a result of a density and refractive index modification due to the oxide layer, requiring treatment of these samples as porous-SiO_2 glass films [35].

The elastic constants, including Young's modulus, were calculated for a p^+ type sample demonstrating a decrease in elastic constants as compared to c-Si [36]. Andrews *et al.* reported an increase in porosity of low resistivity samples with decreasing HF concentration in the electrolyte and noted a decrease in surface phonon velocity with increasing porosity [37]. In a follow up report, the elastic constants and Young's modulus were reported for a p^+, p^-, and n^+ sample, all with similar porosities. It was shown that due to distinct pore/crystallite geometries and morphologies, the phonon velocities, elastic constants, and Young's modulus for the p^+ sample were 1.6, 2.8, and 2.7 times higher than for the p^- film, respectively [38].

1.3 Bioactivity of Porous Silicon

The potential use of π-Si as a biomaterial, based on its bioactivity, was first reported by Canham in Ref. [39]. A bioactive material implanted into living tissue may form a direct chemical bond with bone and soft tissue. This bond reduces the likelihood of prolonged inflammation and promotes complete integration of the implant with the rest of the body [40]. Porous silicon films have been shown to induce hydroxyapatite (HA, the naturally occurring mineral component of bone) growth in simulated

body fluid (SBF), defined in the following paragraph, suggesting the potential to bond directly to living soft tissue and bone. It has been speculated that the speed of hydroxyapatite nucleation in SBF on the silicon structure could be significantly accelerated by optimizing the π-Si film properties such as porosity, pore morphology, and surface area [39]. Further, in comparison to titanium, porous silicon implants have been shown to elicit comparable reactions [41].

Simulated body fluid is an acellular solution containing inorganic ion concentrations similar to those in human blood plasma [42]. Immersing a bioactive substance in SBF induces precipitation of the mineral phase of bone, hydroxyapatite ($Ca_{10}(PO_4)_6(OH)_2$), on its surface. The rate at which calcium phosphate deposits develop on a material's surface and transform to HA has been used to gauge the level of bioactivity of the material [40]. Using scanning electron microscopy (SEM) and energy dispersive X-ray (EDX), it was demonstrated that in as little as 7 days sphere-like particles, characteristic of apatite growth were found on the surface of the porous silicon [39]. Further aiding in the candidacy for use as a biomaterial, when compared to other bioactive materials, such as bioglass [43, 44], Si toxicology data suggests it is a trace nutrient in human blood plasma and serum in the water soluble form of silicon, orthosilicic acid, $Si(OH)_4$. This aqueous form of silicon has also been demonstrated to be optimal in bone and collagen growth as it stimulates calcification and creates a negligible inflammatory response [39, 45].

Pramatarova *et al.* studied the deposition of HA on porous silicon films using a

simple soak method, where the samples are immersed in SBF at 37°C for 15 hours, and a laser-liquid-solid interaction (LLSI) procedure, where a scanning laser promotes synthesis in a localized area [46–48]. This method allows interaction between a scanning laser and the film immersed in the SBF to promote and enhance HA nucleation [48]. Their report showed that the layers of HA deposited via the simple soak were dense and homogenously distributed, whereas the LLSI method resulted in a thin layer of calcium and phosphorous, and randomly distributed clusters of HA [48]. In Ref. [49] a cathodic bias was applied to promote HA precipitation, as originally proposed in Ref. [40]. The negative polarization of the π-Si provoked degradation of the porous structure with simultaneous growth of HA around sites of H_2 evolution. For samples with Ca and P deposits already on the surface, the negative bias promoted further growth covering the entire surface [49]. The incorporation of transition metal complexes into the porous silicon-hydroxyapatite framework providing molecular recognition has also been reported [50]. Li *et al.* employed cathodic bias-induced nucleation in the presence of the desired transition metal complex, resulting in deposits consistent with the characteristics of HA. Demonstration of the fabrication of a nanoporous silicon film containing calcium phosphate was reported using a spark processing method where a high-frequency arc from a Tesla coil is used to ablate the silicon surface containing an excess coating of HA [51, 52]. It is demonstrated that films as thick as 20 μm can be formed. Overall, further research is required to determine the factors influencing HA deposition in order to promote bone-mineral growth

for ideal scaffold fabrication.

The effect of oxidation on porous silicon bioactivity has also been reported. Pastor *et al.* studied the effect that surface modification of mesoporous silicon samples has on the bioactivity [53]. Carbonized porous silicon samples, with Si-H_x bonds replaced by Si-C bonds by immersion in C_2H_2 at 500°C, were demonstrated to be bioinert. After oxidizing the carbonized porous silicon samples, HA deposits were noted on the surface when re-immersed in SBF [53]. Further, it has been reported that a 70% mesoporous film with a surface area approximately 640 m^2/g was completely dissolved in about 24 hours, whereas low to medium porosity microporous films, oxidized by extended storage in ambient air, were much more stable [39]. Further, in Ref. [49] it was shown that after 15 days immersion in SBF, the oxidized porous silicon film displays HA deposits whereas the unoxidized film does not [53].

The osteoconductivity, or ability to support and promote osteoblast growth, of porous silicon films of with differing pore sizes ($<$ 20 nm, 50 nm, and 1000 nm) has also been studied [27, 54]. Sun *et al.* demonstrated that different π-Si architectures induced differing cellular response [27]. Specifically, macroporous silicon best supported osteoblast growth and best sustained cell function, with resulting cell morphology and function similar to those grown on polystyrene culture plates as a control [27]. The increased function and viability on macroporous silicon was attributed to the different morphology of the cell-substrate interface, speculating that local geometries at cell contact points deliver different mechanical signals to the cell,

initiating different cellular response.

1.4 Present Work

In this work porous silicon films with pore diameters ranging from a few nanometers to a few microns are fabricated on p^-, p^+, and n^+ type bulk silicon. For p^- type samples, the relationship between the resulting porosity and both the hydrofluoric acid concentration in electrolyte and resistivity of the bulk silicon are reported and compared to previously reported data.

The fabrication of macroporous silicon films, formed on p^- type bulk silicon, is demonstrated. The effect of the current on the resulting pore diameter in an organic electrolyte containing acetonitrile is reported for the first time.

Brillouin light scattering experiments are used to determine the phonon velocities of p^- and n^+ type silicon films. These results allow the calculation of the elastic constants, the Young's modulus, and the bulk modulus for each film. Few Results have been reported on the elastic constants of p^- type microporous silicon films with porosity range of 59% - 85%. Knowledge and control of the elastic properties of bioactive porous silicon films permits future use as a bioactive material in the field of tissue engineering. Knowledge of the mechanical properties of the porous silicon films will allow fabrication of a scaffold of which the elastic constants match those of the desired tissue.

The dissolution of micro-, meso-, and macroporous silicon films in simulated body

fluid is reported, allowing prediction of the dissolution of these films based on the sample surface area. Knowledge of the rate of breakdown of the porous film in SBF is required in biomaterial applications. Further, the bioactivity of macroporous films is demonstrated through the deposition of hydroxyapatite on its surface studied by EDX and SEM techniques.

These studies provide a basis for the use of porous silicon as a bioactive and elastically-adjustable bone-building matrix.

Chapter 2

Film Fabrication

One of the primary reasons for the broad range of applications of porous silicon, from optoelectronics to drug delivery, is the available tunability of the films properties, including the porosity and elastic moduli [55]. The characterization of porosity as a function of etching parameters, such as the current density, HF concentration and time, allows the fabrication of films of approximate known porosity. In this chapter microporous, mesoporous, and macroporous silicon films, formed from p^- and n^+ type wafers are reported and characterized. For microporous samples, the porosity as a function of hydrofluoric acid concentration in electrolyte and bulk silicon wafer resistivity is reported for the first time on substrates with resistivities in the range 2.5 - 4.0 Ω·cm. The porosity of mesoporous silicon samples, formed on n^+ type bulk wafers, was determined using a gravimetric and optical method. SEM studies of macroporous silicon samples fabricated on p^- type films using an organic electrolyte

are presented confirming the formation of macropores. The first study of the effect of the applied current during the anodization process on the resultant average pore diameter is reported. Overall it is demonstrated that a wide range of achievable pore sizes and porosities are available, a requirement for an ideal tissue engineering scaffold.

2.1 Electrochemical Etching

Porous silicon was fabricated by electrochemical etching of crystalline silicon in an electrolyte containing hydrofluoric acid. The [100]-oriented pieces of crystalline silicon for electrochemical etching were cleaved from full discs using a diamond scribe to fit into a teflon electrolytic cell, shown in Figure 2.1a. To remove any native oxide on the surface, the cleaved pieces of crystalline silicon were placed in hydrofluoric acid for 60 seconds before etching. The copper electrode below the sample, as shown in Figure 2.1a, was connected to the positive terminal of a Keithley 2400 SourceMeter programmable constant current source, and the platinum electrode, above the sample was immersed in the electrolyte and connected to the negative terminal. A Fluke 87 V digital multimeter was used to monitor the current supplied to the cell. This setup is shown in Figure 2.1b. Anodization was performed in darkness to minimize the effects of photochemical etching [56]. It is notable that 1.4 cm^2 of the silicon was exposed to the electrolyte during fabrication. After etching the sample was rinsed in water and then immersed in pentane for 60 seconds. Pentane is used as a drying

agent as it has a low surface tension which prevents cracking and has no chemical interaction with the porous silicon layer [57].

2.2 Microporous Silicon

Microporous silicon films were formed in electrolytes with HF concentrations between 20% - 45% from p-type silicon wafers with resistivity in the range 2.5 - 4.0 Ω·cm or 9.0 - 13.0 Ω·cm. Sample fabrication conditions are given in Table 2.1.

The porosity of the microporous silicon films was determined optically through the measurement of the Brewster angle, θ_B, as described in [55]. Measurements were carried out with TM-polarized light from an Nd:YVO_4 laser ($\lambda = 532$ nm) incident on the sample mounted on a rotation stage as shown in Figure 2.2. The incident light intensity was measured using a photodiode (OptiSci Photoreceiver Module) with no sample present. The intensity of the reflected light from the sample was measured as a function of the incident angle, allowing the angle corresponding to the reflectance minimum to be recorded. From this method the refractive index, n, is found using

$$n = \tan \theta_B. \tag{2.1}$$

The porosity, ξ, of the films was then determined using the two-component Brugge-

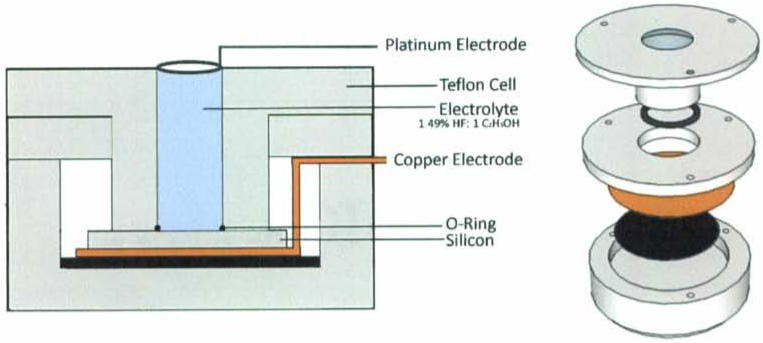

(a)

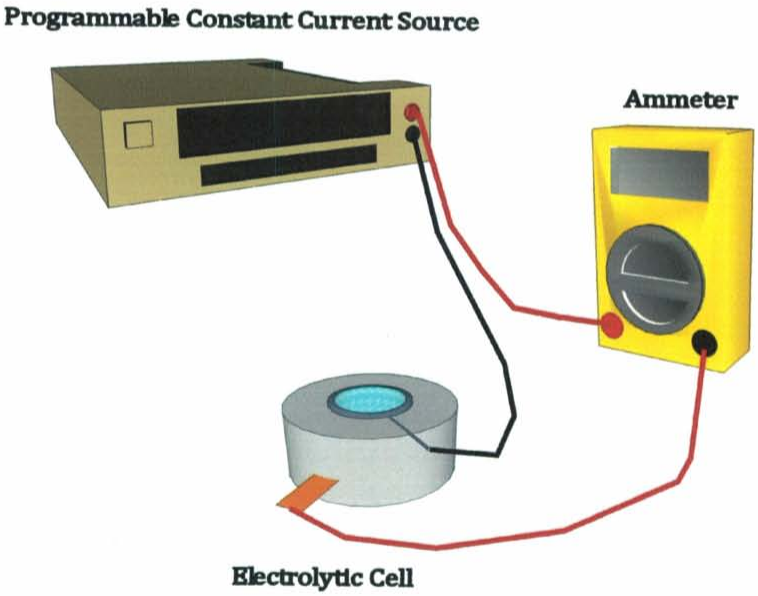

(b)

Figure 2.1: a)Cross section of Teflon electrolytic cell, b)Electrochemical etching fabrication setup.

Table 2.1: Etching conditions and resultant porosity of microporous silicon on p^- type substrate. ([1]: $\xi_{Gravimetric} = 0.69$, [2]: $\xi_{Gravimetric} = 0.70$ determined using Equation (2.3))

Sample	Resistivity (Ω·cm)	I (mA)	t (s)	HF : C_2H_5OH	ξ ($\pm$ 0.02)
3.15#10	2.5 - 4.0	15	300	12 : 1	0.59
3.16#8	2.5 - 4.0	10	900	9 : 1	0.65
3.16#9	2.5 - 4.0	10	900	9 : 1	0.63
3.17#3	2.5 - 4.0	15	900	9 : 1	0.62
3.17#4	2.5 - 4.0	15	900	9 : 1	0.60
3.15#2	2.5 - 4.0	15	420	3 : 1	0.59
3.15#3	2.5 - 4.0	15	420	2 : 1	0.62
3.15#11	2.5 - 4.0	15	300	2 : 1	0.66
3.16#1	2.5 - 4.0	28	600	1 : 1	0.74
3.16#12	2.5 - 4.0	28	600	1 : 1	0.73
3.15#13	2.5 - 4.0	28	600	1 : 1	0.74[1]
5.2#15	9.0 - 13.0	28	600	1 : 1	0.71
5.2#16	9.0 - 13.0	28	600	1 : 1	0.75
5.2#12	9.0 - 13.0	28	300	1 : 1	0.75[2]
3.16#4	2.5 - 4.0	15	900	1 : 1	0.73
3.16#5	2.5 - 4.0	15	900	1 : 1	0.76
3.16#12	2.5 - 4.0	28	600	1 : 1	0.72
3.17#5	2.5 - 4.0	10	900	1 : 1	0.74
3.17#6	2.5 - 4.0	10	900	1 : 1	0.73
3.15#5	2.5 - 4.0	15	600	1 : 1.5	0.81
3.16#3	2.5 - 4.0	25	900	1 : 1.5	0.86
3.16#10	2.5 - 4.0	15	900	1 : 1.5	0.84
3.16#11	2.5 - 4.0	15	900	1 : 1.5	0.83
3.17#1	2.5 - 4.0	10	900	1 : 1.5	0.85
3.17#2	2.5 - 4.0	10	900	1 : 1.5	0.84
3.15#7 GaIn	2.5 - 4.0	45	300	1 : 1	0.80
3.15#8 GaIn	2.5 - 4.0	15	420	1 : 1	0.76

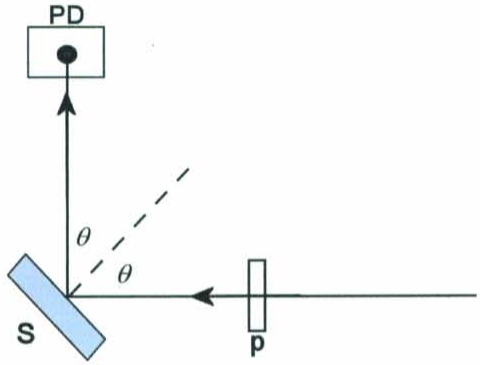

Figure 2.2: Optical reflectance apparatus. p - Polarizer, S - Sample on rotation stage, PD - Photodiode.

mann effective medium model [58]

$$\xi = 1 - \frac{(1-n^2)(N^2+2n^2)}{3n^2(1-N^2)} \tag{2.2}$$

where n is the refractive index of the porous film and N is the refractive index of crystalline silicon ($N = 4.22$ at 532 nm). It is important to note that this method is only valid for samples in which the complex part of the refractive index can be ignored and samples which are optically isotropic.

It is well known that for a given electrolyte concentration the resultant porosity is independent of the applied current for p^- type silicon samples with resistivity greater than approximately 1 Ω·cm [7, 18, 23]. However, it has also been shown that the resultant porosity of p-type films can be controlled by manipulating the HF concentration in the electrolyte [8,23,38]. Figure 2.3 is a plot of porosity as a function

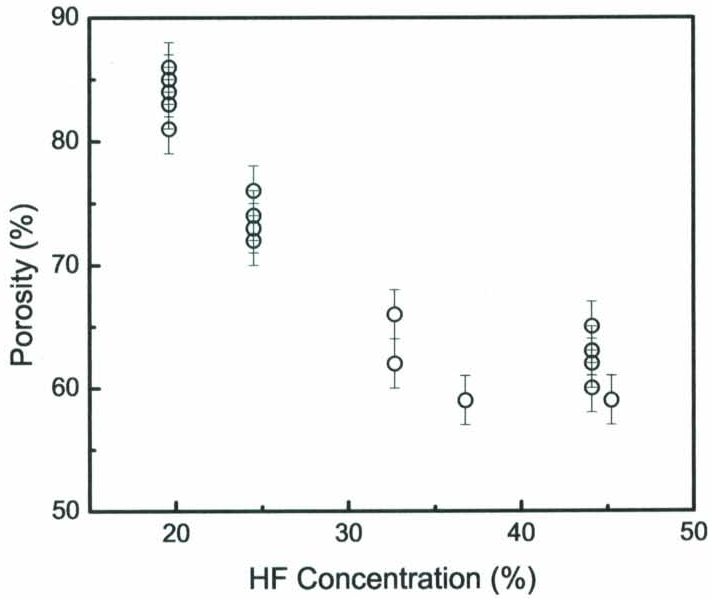

Figure 2.3: Film porosity versus hydrofluoric acid concentration in an electrolyte containing Hydrofluoric acid and ethanol for p^- samples.

of the HF concentration in an electrolyte containing only 49% HF and C_2H_5OH. As is evident in this plot, film porosity decreases with increasing HF concentration.

Samples fabricated in an electrolyte containing 19.6% HF (1 (49%) HF : 1.5 C_2H_5OH) resulted in films with porosities in the range of 81% - 85%. At lower HF concentrations in the electrolyte, including 16.3% (1 (49%) HF : 2 C_2H_5OH), no porous layer was formed, instead, electropolishing of the porous layer occurred. Electropolishing was also reported by Herino et al. [21] in an electrolyte containing 24.5% HF on a 17 Ω·cm substrate. However, in a 12.3% HF electrolyte concentration Fan *et*

al. reported formation of a 83% porous silicon film on 1.48 - 1.84 Ω·cm bulk silicon. Comparing these three results, the resistivity of the bulk silicon has an obvious effect on the minimum HF concentration to allow pore formation.

Samples fabricated with an electrolyte containing 24.5% HF (1 (49%) HF : 1 C_2H_5OH), and 44.1 % HF (9 (49%) HF : 1 C_2H_5OH) resulted in porous silicon with porosity ranges determined to be 72% - 76% and 60% - 65 %, respectively (see Table 2.1). Andrews *et al.* reported a sample with porosity of 59% on p-type silicon with resistivity of 5.1 - 6.9 Ω·cm in an electrolyte with a HF concentration of 34.3% [38]. The porosity of the samples fabricated by Andrews is lower than presented in this study and can be attributed to the higher resistivity range of the bulk silicon used. This relationship of decreasing porosity with increasing sample resistivity for p^- type silicon has been documented [8, 21]. Bellet *et al.* [31] reported a 70 % porous silicon film fabricated on p-type silicon with resistivity of 5 Ω·cm in a 25 % HF electrolyte and Herino [21], using the same resistivity silicon and HF concentration a 71% sample is formed. Both results are slightly lower than presented here, which can be attributed again to the sample resistivity. It is also shown in Ref. [21] for a set of samples fabricated on p-type silicon with resistivity of 17 Ω·cm with HF concentration between 25% and 55 % that as HF concentration increases, porosity decreases. These results are plotted in Figure 2.4, along with the other results discussed in this section. For all data presented in Figure 2.4 it can be seen that as HF concentration in the electrolyte increases, porosity decreases.

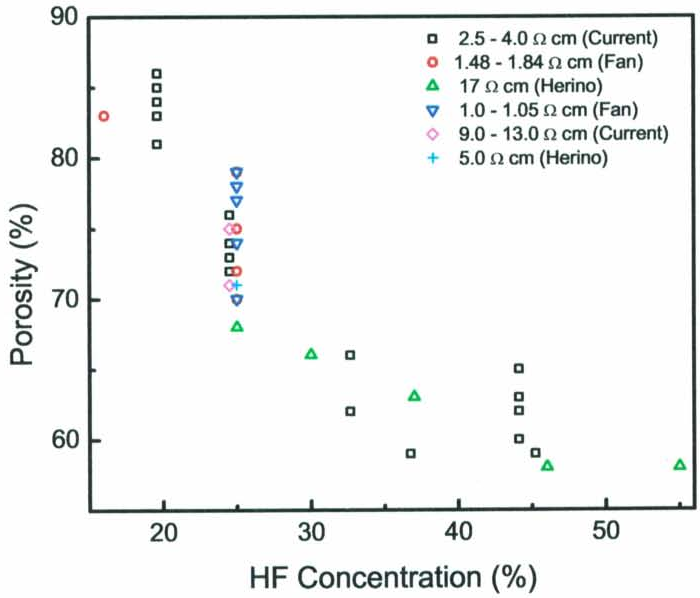

Figure 2.4: Porosity versus HF concentration for porous silicon films formed from p^- type parent wafers of different resistivity.

As shown in Table 2.1, two samples were fabricated using bulk silicon with resistivity range 9.0 - 13.0 Ω·cm in an electrolyte containing 24.5% HF. It was expected that the porous silicon films fabricated on the 9.0 - 13.0 Ω·cm substrate would have a lower porosity than films formed on 2.5 - 4.0 Ω·cm substrates under the same conditions. Instead, the porosities of the samples were found to be 71% and 75%. These porosity values are similar to those of films formed on 2.5 - 4.0 Ω·cm substrates in this work, and the other reported samples fabricated on 5 Ω·cm [21,31]. These results are plotted in Figure 2.5 for samples formed in an electrolyte containing $\sim$ 25% HF.

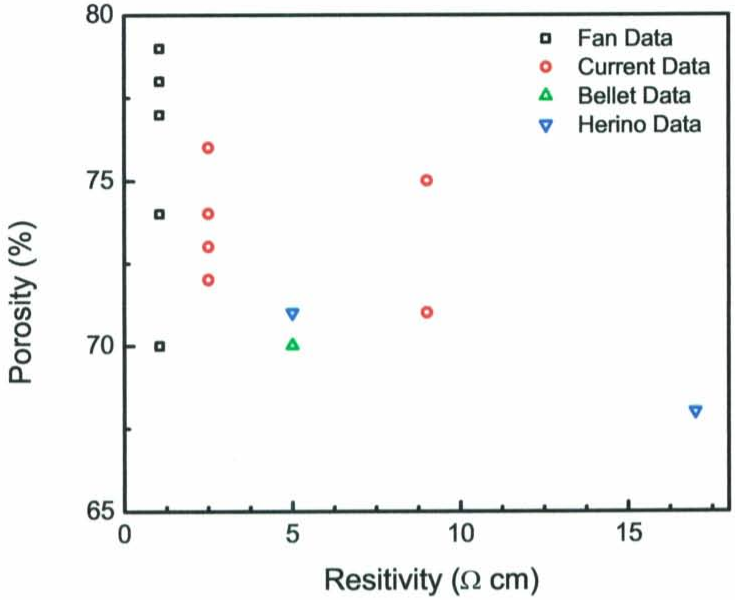

Figure 2.5: Porosity versus resistivity for porous silicon films fabricated from p^- type crystalline silicon wafers. The HF concentration in the electrolyte was $\sim 25\%$.

To determine the effect of Gallium-Indium (GaIn) eutectic on the resulting microporous films, two samples, see Table 2.1 samples 3.15#7 and 3.15#8, were backside coated with Gallium-Indium eutectic before being placed in the cell. The appearance of the resultant films differed from those typically prepared under the same etching conditions. A value for the porosity was determined optically by fitting the Fresnel equation to the scattered data collected for the reflectance versus incident angle.

Table 2.2: Etching conditions and resultant porosity of mesoporous silicon films formed on n^+ type silicon substrates in an electrolyte containing 1 (49%) HF : 1 C_2H_5OH.

Sample	Current (mA)	Time (s)	$\xi_{Gravimetric}$ (%)
1.17#5	4.2	360	41
1.17#6	28	240	36
1.17#7	42	132	28
1.18#1	56	120	27
1.18#2	84	90	25
1.17#1	20	600	39
1.17#2	40	420	50

2.3 Mesoporous Silicon

Mesoporous silicon films were formed on n^+ type substrates with resistivity in the range of 0.005 - 0.02 Ω·cm in an electrolyte containing 1 (49%) HF and 1 C_2H_5OH with currents ranging from 4.2 mA - 84 mA. Detailed etching conditions are given in Table 2.2. For these samples, for comparison purposes, the porosity was determined gravimetrically using

$$\xi_{Gravimetric} = \frac{m_1 - m_2}{m_1 - m_3}, \tag{2.3}$$

where m_1 is the mass of the c-Si sample prior to porous film formation, m_2 is the mass of the sample after porous film formation, and m_3 is the mass of the sample after the porous region is selectively removed by immersing the sample in 1% KOH solution for approximately 90 s. The selectivity of KOH to π-Si is possibly due to the fact that the total surface area of the porous region is much larger than that of the crystalline region. Figure 2.6 shows a representation of this process.

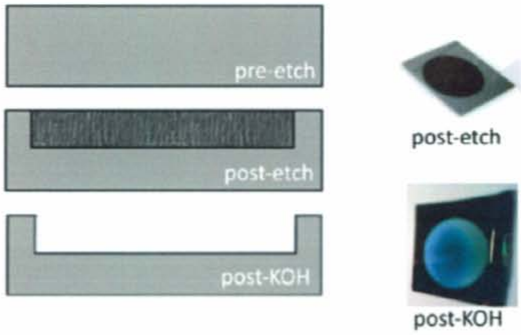

Figure 2.6: Illustration of cross section of samples before etching, after etching, and after immersion in KOH. Pictures of samples after etching, showing porous region (dark area), and after KOH, showing removed porous region.

The porosities of the mesoporous n^+ type samples fabricated under these etching conditions determined using Equation (2.3) disagrees with those porosity values determined optically as described previously in Sec. 2.2, leading to the conclusion that the optical method is not valid. This is an expected result as it has been demonstrated that under these conditions the resultant sample is mesoporous, with ordered columnar pores of diameter 10 - 120 nm [8]. These samples are therefore not optically isotropic, and hence the optical method is not valid. The gravimetric method is a more universal method in determining porosity but requires sample destruction with a higher error, especially for thin films, when compared to the optical method. Further discussion on this topic can be found in [55].

2.4 Macroporous Silicon

Macroporous silicon was fabricated in an electrolyte of 1 (49%) HF : 14 Acetonitrile (ACN) on p^- type silicon wafers with resistivity range 9.0 - 13.0 Ω·cm using the same set-up as previously described. All samples were fabricated using a current of 14 mA unless otherwise stated. The silicon wafers were backside coated with GaIn eutectic before being placed in the cell [24].

The formed samples were studied using scanning electron microscopy. Average pore size for each sample were determined for a random selection of ten pores using an image analysis program (Corel Paint Shop Pro Photo X2) for each sample.

The formation of macroporous silicon on p-type low doped substrates, as low as 2 - 3 Ω·cm, is well documented in [24, 26, 59–61]. In all of the previously mentioned studies, the electrolyte used in the fabrication process contains an organic component, namely acetonitrile (ACN), propylene carbonate (PC), dimethylformamide (DMF), or dimethylsulfoxide (DMSO). The only reported exception to the previous statement is found in Ref. [59] which states that an organic component is not required in the electrolyte. Lehmann *et al.* produced macroporous films on p-type samples with resistivity of 20 Ω·cm in an aqueous electrolyte with an HF concentration of 30 %. In this work the results of Lehmann *et al.* could not be replicated, possibly due to a difference in substrate resistivity. The organic component of the electrolyte used here was ACN, chosen based on a lower overall electrolyte resistivity as compared to DMF, $\sim$ 2200 Ω·cm and $\sim$ 5300 Ω·cm, respectively, for the typical volumes used by

this group [61]. It is notable, however, that using DMF a porous layer is achievable on p-type substrate with resistivity of 0.2 Ω·cm [60]. The role of the organic component of the electrolyte in macropore formation is not well understood. More information on the organic component role can be found in [62].

The macroporous silicon studied in this work had an average pore size of approximately 1.2 - 1.8 μ m as shown in Figure 2.7. Samples fabricated on substrates comparable to that used in this study resulted in pores with average diameter of 1.2 μm [60], 1.6 μm [61], and 1.4 μm [26].

Further, it is noted in the cited work on this topic that when using an organic electrolyte a thin, cracked microporous layer is present above the desired macroporous layer, with the exception of an organic electrolyte containing DMF [61]. SEM images of such a layer are shown in Figure 2.8. Figures 2.8a and 2.8b are SEM images of the surface of samples which were partially dipped in KOH to remove the microporous layer of half of the sample. The boundary is clearly evident. In Figures 2.8c and 2.8d the holes and cracks in the microporous layer are evident, and are not the result of any KOH etching.

The effect of crystal orientation, silicon doping density, and electrolyte composition on resultant macropore morphology has been well studied and is summarized in Ref. [25]. However, little work has been done on the effect of the applied current on the resultant film. Figure 2.9 presents SEM images of the film surface for currents of 3 mA, 5 mA, 7 mA, 9 mA, and 14 mA. From Figure 2.9a it is obvious that at 3

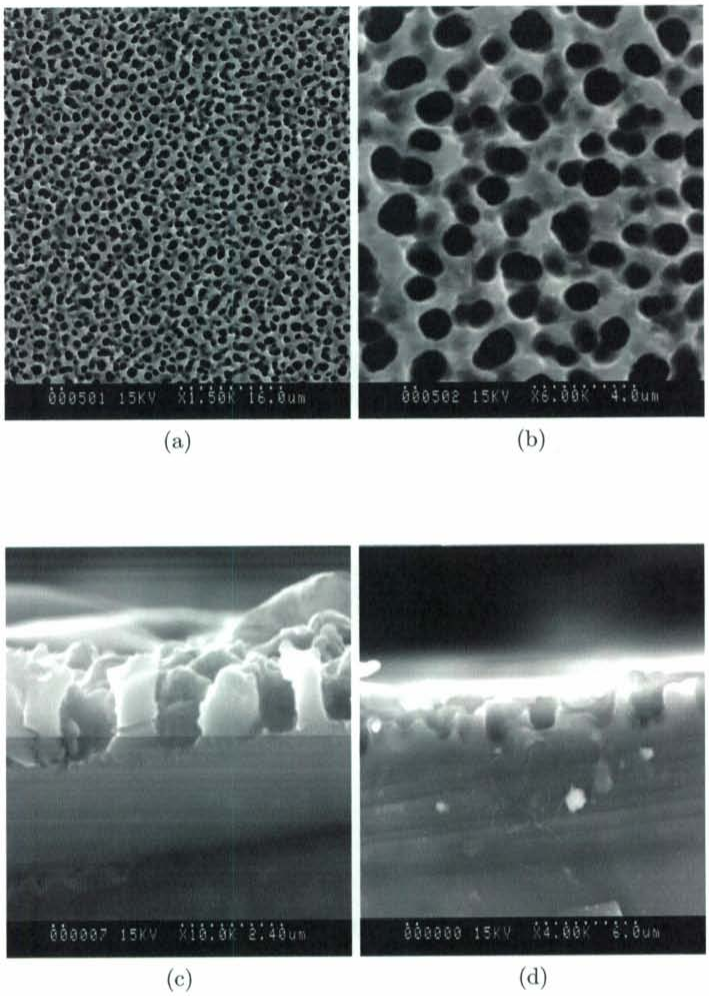

(a) (b)

(c) (d)

Figure 2.7: SEM images of the surface of macroporous silicon a) at 1500 X magnification, and b) at 6000 X magnification. Cross sectional SEM images of the macropores c) at 10000 X, and f) at 4000 X.

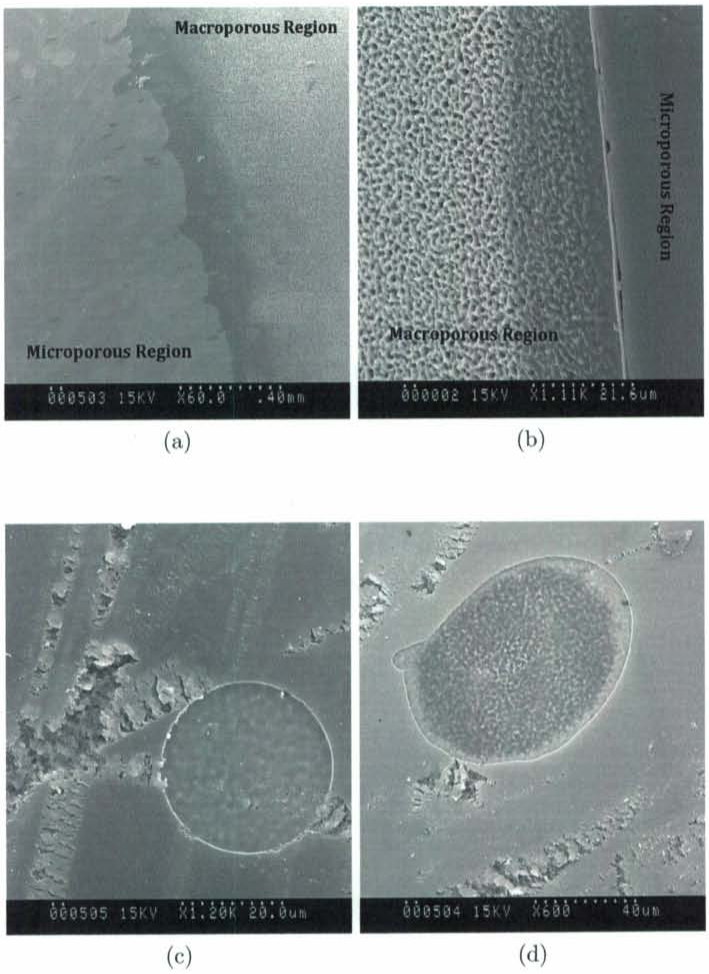

Figure 2.8: SEM images of the microporous silicon layer formed above the macroporous layer below. a) and b) show the boundary of the microporous film covering the macroporous layer. The microporous layer was removed in KOH. c) and d) show the cracked microporous layer.

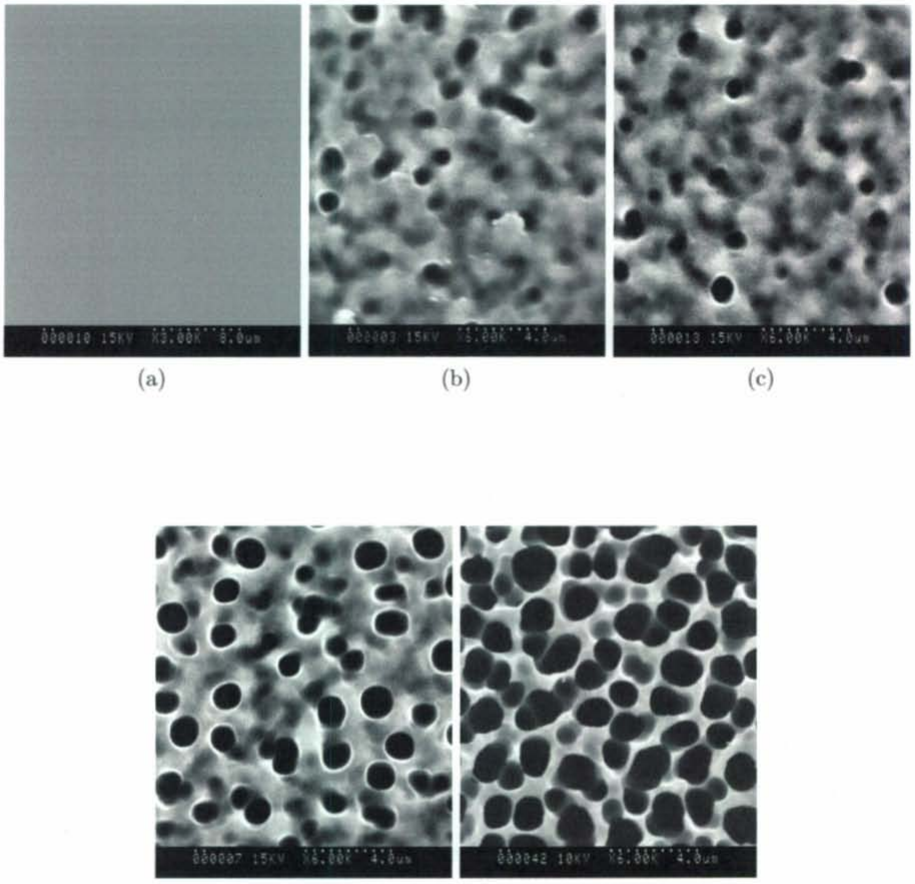

(a) (b) (c)

(d) (e)

Figure 2.9: SEM images of a) no macroporous film formed with I = 3 mA, and macroporous silicon formed for at b) I = 5 mA, c) I = 7 mA, d) I = 9 mA, and e) I = 14 mA.

Table 2.3: Etching current and resultant average pore diameter of macroporous silicon samples from in an electrolyte of 1 (49%) HF : 14 ACN

Current (mA)	Average Pore Diameter (μm) ($\pm$ 5%)
3	-
5	0.9
7	1.2
9	1.3
14	1.8

mA no macroporous film is formed. Comparing figures 2.9b - 2.9e it is seen that as the current increases, the pore diameter increases. It also seen that as the pore size increases, the density of pores increases, and the thickness of the pore walls decreases, as has been demonstrated previously [26]. Table 2.3 presents the resultant average pore sizes determined using image analysis software for a random selection of 10 pores per sample. Fitting to the data in Figure 2.10 reveals an approximate linear relation between pore diameter and applied current density for the range of currents studied ($d_{pore} = 0.13 \cdot j + 0.46$). The formation of macroporous silicon with currents greater than 14 mA was not attempted. Based on the decreasing pore wall size seen in Figure 2.9 it is expected that further increase in current would result in complete destruction of the film.

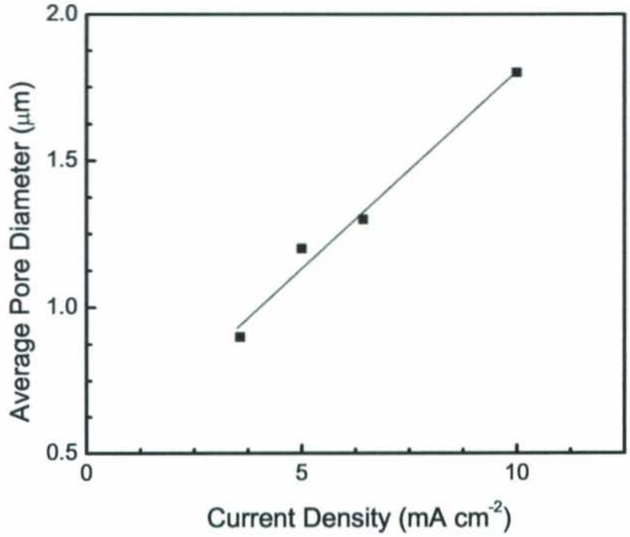

Figure 2.10: Average pore size of macroporous samples as a function of current density for samples fabricated from p^- type bulk silicon in an electrolyte containing 1 49% HF : 14 ACN.

Chapter 3

Elastic Properties of Microporous Silicon Films

Brillouin light scattering spectroscopy is a powerful tool for determining the elastic properties of semiconductors. It is complementary to ultrasonic techniques in determining the elastic properties, without the need for external contact with the material [14]. The mechanical properties of materials are determined using Brillouin light scattering through interaction of photons and acoustic phonons in the target material. Brillouin light scattering has been used in this work to characterize the phonon velocities and elastic constants for p^- type and n^+ type porous silicon films.

3.1 Theory

3.1.1 Brillouin Light Scattering

The inelastic scattering of light in a material due to interactions with acoustic modes is referred to as Brillouin light scattering. In this process a photon exchanges energy and momentum with a phonon, or lattice vibration, changing the energy and momentum of the scattered photon [63]. In quantum mechanics terminology the process is a first order scattering by acoustic phonons [64]. The energy and momentum of a photon respectively are

$$E = \hbar\omega \tag{3.1}$$

and

$$p = \hbar\mathbf{k} \tag{3.2}$$

where ω is the angular frequency and $\mathbf{k}$ is the wavevector. Similarly, for a phonon the energy and momentum are given as

$$E = \hbar\Omega \tag{3.3}$$

and

$$p = \hbar\mathbf{q} \tag{3.4}$$

where Ω is the angular frequency and $\mathbf{q}$ is the wavevector.

By the laws of conservation of energy and momentum, respectively, during the scattering process

$$\hbar\omega_i = \hbar\omega_s \pm \hbar\Omega \tag{3.5}$$

and

$$\hbar\mathbf{k}_i = \hbar\mathbf{k}_s \pm \hbar\mathbf{q} \tag{3.6}$$

where the subscript i represents the incident light and the subscript s represents the scattered light [65, 66].

The result of the interaction between an acoustic phonon and an incident photon is one of two types of scattering, phonon creation or annihilation, which corresponds to the positive and negative signs in Equations (3.5) and (3.6) respectively. For a process where the scattered photon's angular frequency is less than the incident photon's angular frequency ($\omega_s < \omega_i$), phonon creation occurs due to the fact that energy from the incident photon is used to create the phonon. In the process of phonon annihilation, the scattered photon's angular frequency will be greater than that of the incident photon ($\omega_s > \omega_i$), since the phonon is absorbed [63]. Phonon creation and annihilation correspond to the so-called Stokes and anti-Stokes component of the scattered radiation, respectively [64]. As a result, a scattered light spectrum contains peaks with both positive and negative frequency shifts from the incident light frequency [56]. In general, it is found for isotropic materials that peaks due to two acoustic bulk modes are observed in a Brillouin spectrum, a longitudinal and

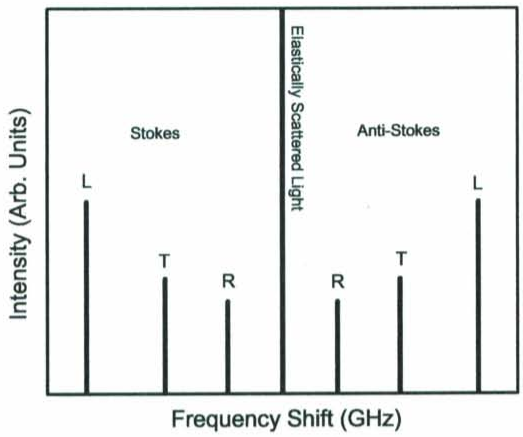

Figure 3.1: Schematic of a Brillouin light scattering spectrum. Peak labels: R - Rayleigh surface mode, L - longitudinal mode, T - transverse mode.

a transverse, as well as a surface mode, also known as a Rayleigh surface mode, as shown in Figure 3.1. The prominent central line assigned zero frequency shift is due to elastically scattered light.

From Equation (3.5) the frequency of the phonon is equivalent to the frequency shift between the scattered and incident photon. Also, the angular frequency of the phonon can be found using

$$\Omega = v_p q \tag{3.7}$$

where v_p is the phonon velocity in the given solid. The assumption that $\Omega << \omega_i$ can be made since the angular frequency of the phonon is much smaller, approximately 1000 times less, than the angular frequency of the incident photon from which it follows that $k_i \simeq k_s$.

From Figure 3.2 it is found for the bulk acoustic modes

$$q_B^{\parallel} = k_i \sin\theta_i + k_s \sin\theta_s \tag{3.8}$$

and

$$q_B^{\perp} = n(k_i \cos\theta_i' + k_s \cos\theta_s') \tag{3.9}$$

where n is the refractive index of the medium, $q_B^{\parallel}$ is the parallel component of the bulk phonon wavevector, $q_B^{\perp}$ is the perpendicular component of the bulk phonon wavevector, θ_i is the angle between the surface normal and the incident photon, θ_s is the angle between the surface normal and the scattered photon, θ_i' is the angle between the surface normal and the refracted incident photon, and θ_s' is the angle between the surface normal and the refracted scattered photon [67]. From Figure 3.2 it can be shown that Equation (3.8) can also be written as

$$q_B^{\parallel} = n(k_i \sin\theta_i' + k_s \sin\theta_s') \tag{3.10}$$

from Snell's law. The magnitude of the bulk mode wavevector can then be expressed as

$$q_B = (q_B^{\parallel 2} + q_B^{\perp 2})^{\frac{1}{2}}. \tag{3.11}$$

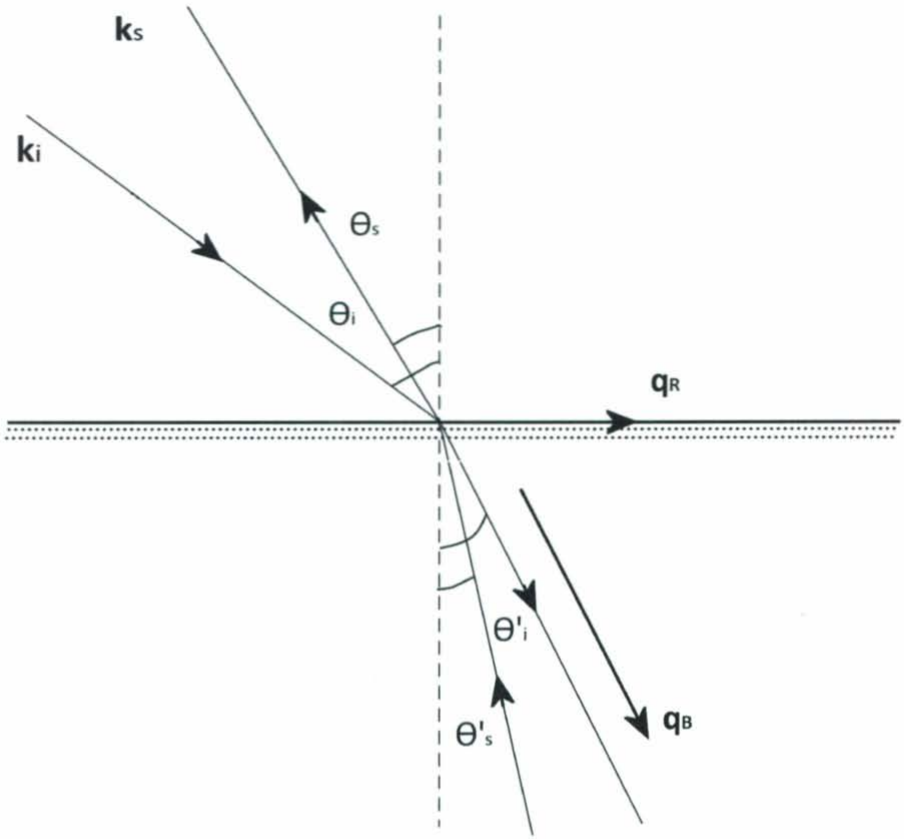

Figure 3.2: Brillouin light scattering from a medium, where $\mathbf{k}_i$ is the wavevector of the incident photon, $\mathbf{k}_s$ is the wavevector of the scattered photon, $\mathbf{q}_R$ is the wavevector of the surface phonon, $\mathbf{q}_B$ is the wavevector of the bulk phonon, θ_i is the angle between the surface normal and the incident photon, θ_s is the angle between the surface normal and the scattered photon, θ_i' is the angle between the surface normal and the refracted incident photon, and θ_s' is the angle between the surface normal and the refracted scattered photon.

Substituting Equations (3.9) and (3.10) into (3.11) one obtains

$$q_B = n(k_i^2 + k_s^2 + 2k_i k_s(\sin\theta_i' \sin\theta_s' + \cos\theta_i' \cos\theta_s'))^{\frac{1}{2}} \tag{3.12}$$

and using the fact that $k_i \simeq k_s$ and manipulating using trigonometric identities it is found that [56, 68]

$$q_B = 2nk_i \cos(\frac{\theta_s' - \theta_i'}{2}). \tag{3.13}$$

For a backscattering configuration such as that used in this work, $\theta_i \simeq \theta_s$, therefore $\theta_i' \simeq \theta_s'$ so

$$q_B = 2nk_i. \tag{3.14}$$

Using Equations (3.7), (3.14), as well as $k_i = \frac{2\pi}{\lambda_i}$ and the relation, $\nu_B = \frac{\Omega_B}{2\pi}$ it is found that the frequency of the bulk acoustic phonons can be written as

$$\nu_B = \frac{2nv_B}{\lambda_i}, \tag{3.15}$$

where v_B is either the transverse phonon velocity, v_T, or the longitudinal phonon velocity v_L.

Rayleigh surface waves penetrate into the bulk over a distance comparable to the acoustic wavelength with a displacement amplitude normal to the surface which decreases exponentially with distance. Therefore, for the perpendicular component, the phonon amplitude decreases to zero a short distance from the surface ($q_R^{\perp}$=0),

conserving only the component parallel to the surface ($q_R = q_R^{\parallel}$) [14]. To determine the frequency of the Rayleigh surface phonons, using the conservation equations, and in accordance with Figure 3.2

$$q_R = k_i \sin\theta_i + k_s \sin\theta_s. \tag{3.16}$$

Once again for a backscattering geometry $\theta_i \simeq \theta_s$, Equation (3.16) becomes [56]

$$q_R = 2k_i \sin\theta_i. \tag{3.17}$$

Since it is known that $k_i = \frac{2\pi}{\lambda_i}$ and the frequency of the surface phonon is given by $\nu_R = \frac{\Omega_R}{2\pi}$, where λ_i is the wavelength of the incident light, the frequency of the Rayleigh surface modes is given as

$$\nu_R = \frac{2v_R}{\lambda_i} \sin\theta_i. \tag{3.18}$$

3.1.2 Elastic Constants

A medium is defined as being elastic if it returns to its initial state after any external forces are removed due to the internal stress of the medium [69]. It is well known that for small deformations the stress, T, is proportional to the strain, S, through Hooke's law as

$$T_{ij} = c_{ijkl} S_{kl} \tag{3.19}$$

where c_{ijkl} is the elastic stiffness tensor with $i, j, k, l = x, y, z$. Since both the stress and strain tensors are symmetric (i.e. $T_{ij} = T_{ji}$ and $S_{kl} = S_{lk}$), the number of elastic constants reduces from 81 to 36 ($c_{ijkl} = c_{jilk} = c_{jilk} = c_{ijlk}$) [64]. Using the previously mentioned symmetries, the subscripts can be relabeled using the Voigt notation such that $\alpha = ij$ and $\beta = kl$, with $1 = xx,\ 2 = yy,\ 3 = zz,\ 4 = yz,\ 5 = xz,\ 6 = xy$ [69,70] changing the rank-four elastic stiffness tensor to

$$\begin{pmatrix} C_{11} & C_{12} & C_{13} & C_{14} & C_{15} & C_{16} \\ C_{12} & C_{22} & C_{23} & C_{24} & C_{25} & C_{26} \\ C_{13} & C_{23} & C_{33} & C_{34} & C_{35} & C_{36} \\ C_{14} & C_{24} & C_{34} & C_{44} & C_{45} & C_{46} \\ C_{15} & C_{25} & C_{35} & C_{45} & C_{55} & C_{56} \\ C_{16} & C_{26} & C_{36} & C_{46} & C_{56} & C_{66}. \end{pmatrix} \tag{3.20}$$

Hooke's law then becomes

$$T_\alpha = C_{\alpha\beta} S_\beta. \tag{3.21}$$

For isotropic media, such as those studied here, the symmetry reduces the number of independent elastic constants to just two such that the elastic constants tensor takes

the form [71]

$$\begin{pmatrix} C_{11} & C_{12} & C_{12} & 0 & 0 & 0 \\ C_{12} & C_{11} & C_{12} & 0 & 0 & 0 \\ C_{12} & C_{12} & C_{11} & 0 & 0 & 0 \\ 0 & 0 & 0 & C_{44} & 0 & 0 \\ 0 & 0 & 0 & 0 & C_{44} & 0 \\ 0 & 0 & 0 & 0 & 0 & C_{44} \end{pmatrix} \tag{3.22}$$

where $C_{44} = \dfrac{C_{11} - C_{12}}{2}$ [64].

To determine the equation of motion in the material, Hooke's law is related to Newton's second law. Newton's second law is [69]

$$\rho \frac{\partial^2 u_i}{\partial t^2} = \frac{\partial T_{ij}}{\partial x_j} \tag{3.23}$$

where ρ is the density, and $\dfrac{\partial^2 u_i}{\partial t^2}$ is the acceleration along the $i - th$ direction. Using Hooke's law, Equation (3.19), where it is known that $S_{kl} = \dfrac{\partial \mu_l}{\partial x_k}$, the equation of motion becomes

$$\rho \frac{\partial^2 u_i}{\partial t^2} = c_{ijkl} \frac{\partial^2 \mu_l}{\partial x_j \partial x_k}. \tag{3.24}$$

For a plane wave the displacement of a particle in the i-th direction is

$$u_i = u_i^o e^{i(k \cdot r - \omega t)} \tag{3.25}$$

where u_i^o is the polarization of the wave. Substituting Equation (3.25) into Equation (3.24) yields the Christoffel equation

$$c_{ijkl}n_j n_k - \rho v^2 \delta_{il} = 0 \tag{3.26}$$

where if we define $\Gamma_{il} = c_{ijkl}n_j n_k$, we find the general form of the Christoffel equation

$$\Gamma_{il} - \rho v^2 \delta_{il} = 0. \tag{3.27}$$

The values ρv^2 are the eigenvalues of this secular equation [69]

$$|\Gamma_{il} - \rho v^2 \delta_{il}| = 0. \tag{3.28}$$

For an isotropic material the solutions to the characteristic equation, Equation (3.28), gives

$$v_L = \sqrt{\frac{C_{11}}{\rho}}, \tag{3.29}$$

and

$$v_T = \sqrt{\frac{C_{44}}{\rho}} \tag{3.30}$$

where ρ is the density of the medium. In the case of porous silicon, the density is given by $\rho = \rho_{Si}(1 - \xi)$ where ξ is the porosity [23, 70].

3.1.3 Derived Quantities

The ratio of stress and strain is given as Young's modulus, E. For an isotropic medium Young's Modulus is expressed as [23]

$$E = \frac{C_{44}(3C_{11} + 4C_{44})}{C_{11} - C_{44}}. \tag{3.31}$$

Another commonly calculated property for a material is the Bulk modulus, B. The Bulk modulus for an isotropic medium is found using the relation [72]

$$B = \frac{1}{3}(C_{11} + 2C_{12}). \tag{3.32}$$

The reciprocal of the bulk modulus, the compressibility (K), may also be reported ($K = 1/B$) [70].

3.2 Experimental Setup

A schematic of the set-up used for the Brillouin light scattering experiments is shown in Figure 3.3. A Coherent Verdi-V2 diode pumped, frequency doubled (Nd:YVO_4), single mode laser emits a vertically polarized 2.0 W beam at wavelength 532 nm and bandwidth $\sim$ 10 MHz. The light passed through a variable neutral density filter (VNDF), which reduced the beam's power. A half-wave plate (HWP) acted to rotate the plane of polarization by 90° resulting in horizontally polarized light which is

incident on a beam splitter (BS). The reflected portion of the beam was directed through an aperture (A) and reflected off a mirror (M). It then continued through a variable neutral density filter, to allow adjustment of the beam power, and into a tandem Fabry-Perot interferometer. The reflected portion of the beam was used as a reference beam which prevents saturation of the photomultiplier tube when scanning over parts of the spectrum containing intense elastically scattered light. A shutter is used to block the scattered light from the sample for certain frequency ranges, replacing the scattered light with the light from the reference beam. The reference beam is also used to maintain mirror alignment for both interferometers.

The transmitted portion of the light incident on the beam splitter was deviated 90° by a front surface mirror. A filter (F), a beam splitter (BS), and a variable neutral density filter result in a reduction of the beam power to approximately 50 mW. The beam was then incident on a prism (P) where it undergoes total internal reflection. A lens (f) with a focal length of 5 cm and f-number of 2.8 focused the beam onto the sample (S) which was on a rotation stage. Some of the scattered light was collected and collimated by the same lens that focused the incident beam. The scattered light is subsequently focused by a lens (L) with focal length 40 cm onto the input pinhole (d = 450 μm) of the tandem Fabry-Perot interferometer TFP-1 (JRS Scientific). All samples were at room temperature in ambient air during collection of spectra.

The Fabry-Perot interferometer is an optical instrument that uses multiple-beam interference to analyze the frequency of the scattered photons. The incident beam

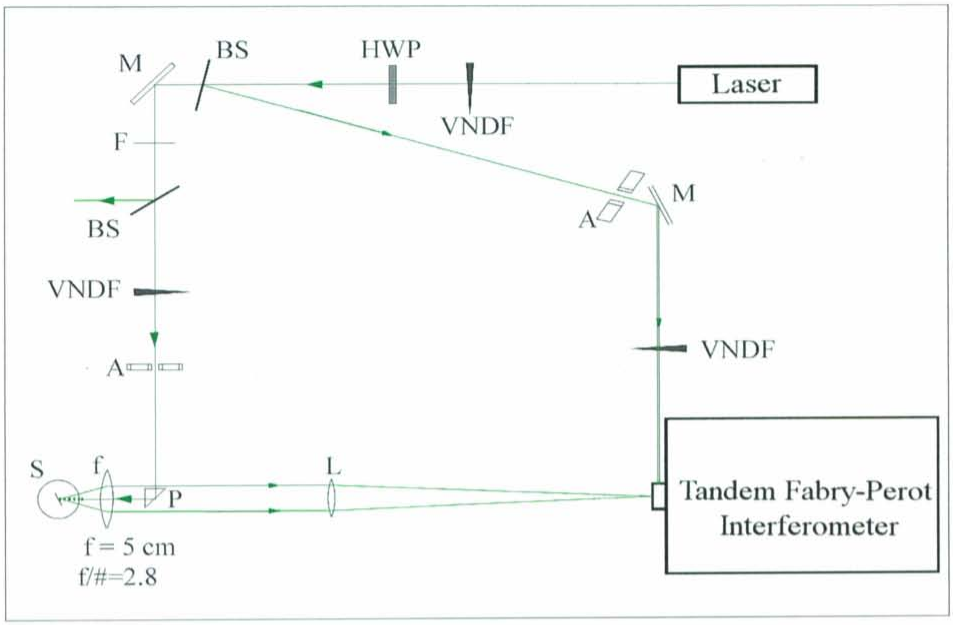

Figure 3.3: Experimental setup. VNDF is a variable neutral density filter, F is an absorbing filter, HWP is a half-wave plate, M is a mirror, A is an aperture, BS and BS' are beam splitters, L is a lens with 40 cm focal length, f is a lens with 5 cm focal length and f-number 2.8, S is a sample on a rotational stage, and P is a prism.

undergoes multiple reflections in an optical cavity consisting of two partially reflective parallel plane mirrors as seen in Figure 3.4. The transmitted wavelengths undergo constructive interference according to

$$2L = m\lambda_i \tag{3.33}$$

assuming that there is perpendicular incidence, where L is the spacing between the mirrors, m is the integral order of interference, and λ_i is the wavelength of the incident

light. By changing the distance between the mirrors, the Fabry-Perot interferometer behaves like a tunable frequency filter. The tandem Fabry-Perot interferometer uses a multipass scheme in which the light passes through each interferometer three times, increasing the contrast. The two interferometers are tilted against each other by an angle α thereby increasing the free spectral range while maintaining a fixed resolution. This is shown in Figure 3.5 for a single pass. The spacings in the optical cavities, L_1 and L_2, are related by

$$L_2 = L_1 \cos\alpha. \tag{3.34}$$

where L_1 and L_2 differ slightly. One mirror of each cavity is mounted on a movable base such that the cavities are scanned simultaneously, therefore satisfying the synchronization condition

$$\Delta L_2 = \Delta L_1 \cos\alpha. \tag{3.35}$$

By moving the base plate, the cavity spacing is changed and the spacing is scanned simultaneously [56, 68, 73]. More information about the Fabry-Perot interferometer may be found in Ref. [74].

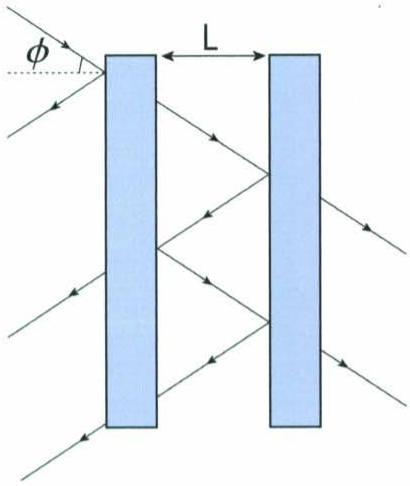

Figure 3.4: Single Fabry-Perot interferometer where L is mirror spacing and ϕ is incident angle of beam entering space.

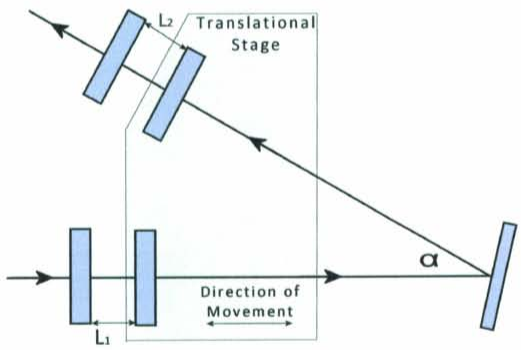

Figure 3.5: Tandem Fabry-Perot interferometer where the light incident on Fabry-Perot 1 passes through, is reflected by a mirror, and is incident on Fabry-Perot 2. The rotational stage moves as shown by the arrows increasing or decreasing the mirror spacings, L_1 and L_2.

3.3 Results and Discussion

3.3.1 Brillouin Spectra of Porous Silicon

Brillouin light scattering experiments were done on p^- type samples with porosities ranging from 59% - 84% and n^+ type samples with porosities of 39% and 50%. The Brillouin spectra for these samples are shown in Figures 3.6 - 3.10, where the peak due to the Rayleigh surface mode is labeled R, the peak due to the transverse mode is labeled T, and the peak due to the longitudinal mode is labeled L. As is well known, the Rayleigh peaks display an angular dependence such that as the angle of incidence is increased, the frequency shift value increases according to Equation (3.13). Further, the bulk mode peaks are seen to be approximately independent of angle of incidence [23]. It is notable that doublet bulk peaks have been observed in some of the spectra. This has previously been noted in Refs. [18, 23] where it was attributed to considerable scattering due to intrinsic inhomogeneity of the c-Si skeleton with the depth of the porous layer.

Frequency shift values corresponding to the maxima of the spectral peaks were determined by fitting Lorentzian functions to the obtained data using graphical analysis software (OriginPro). The resulting data is shown in Tables 3.1 - 3.17 where ν_L, ν_T, and ν_R represent the frequency of the longitudinal, transverse, and Rayleigh surface mode respectively. In the case of doublet peaks, multiple peak Lorentzian fitting was employed, with the peak recurring in multiple spectra for the same sample assigned

to be the peak used for further calculations. In Tables 3.1 - 3.17 the frequency found for these doublets is denoted as ν_{L2}, ν_{L3}, for the longitudinal mode and ν_{T2} for the transverse mode.

It has previously been demonstrated that as the porosity of the sample is increased, the Rayleigh surface and bulk mode frequency shifts decrease. The frequency shift values are plotted as a function of porosity in Figure 3.11 demonstrating the expected trend of decreasing frequency shift with increasing porosity. This result has been well documented on p^+ type samples [37, 64], p^- type samples [23], and n^+ type samples [33]. It is also notable that as the formed samples approach the 80% porosity range, the Rayleigh surface mode peaks become obscured by the shoulder of the central line since the frequency shift values are so small. The FSR was decreased to 20 GHz when collecting spectra for sample 3.15#5, shown in Figure 3.9b, in an attempt to determine the frequency shift of the Rayleigh modes for these high porosity samples. Even with this resolution, a frequency shift value for these peaks could not be determined as they are not visible in the spectra.

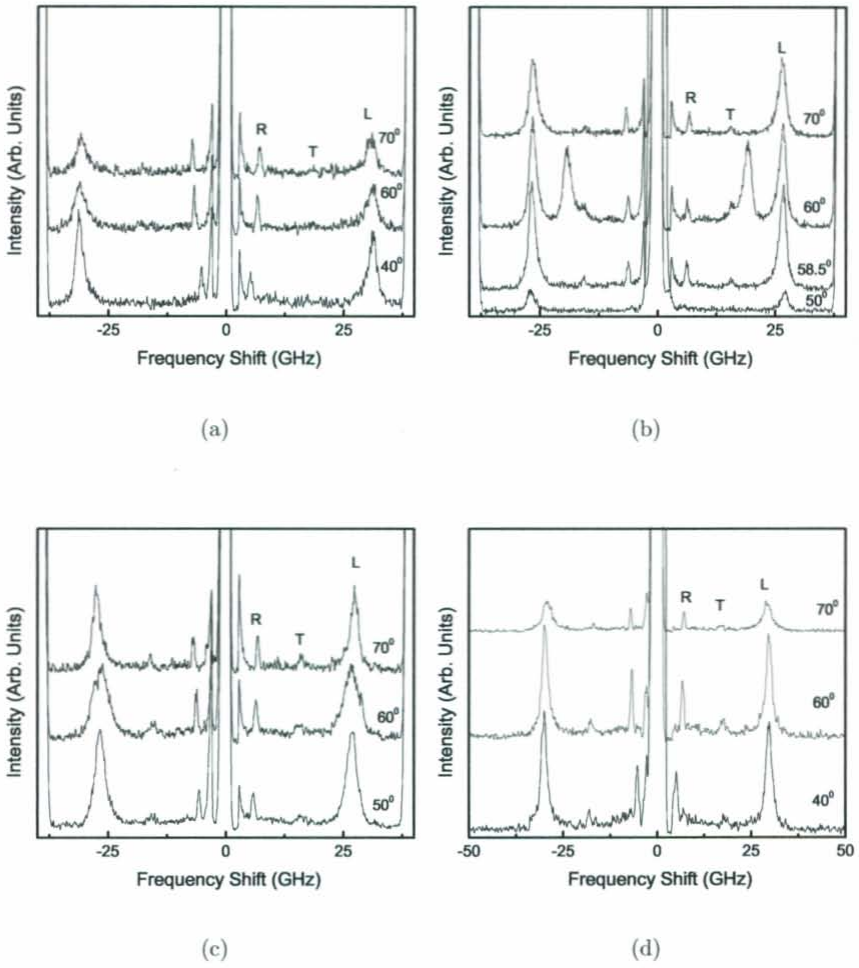

Figure 3.6: Brillouin spectra for a) Sample 3.15#10 with $\xi = 59\%$, b) Sample 3.16#8 with $\xi = 65\%$, c) Sample 3.16#9 with $\xi = 63\%$, and d) Sample 3.15#2 with $\xi = 59\%$.

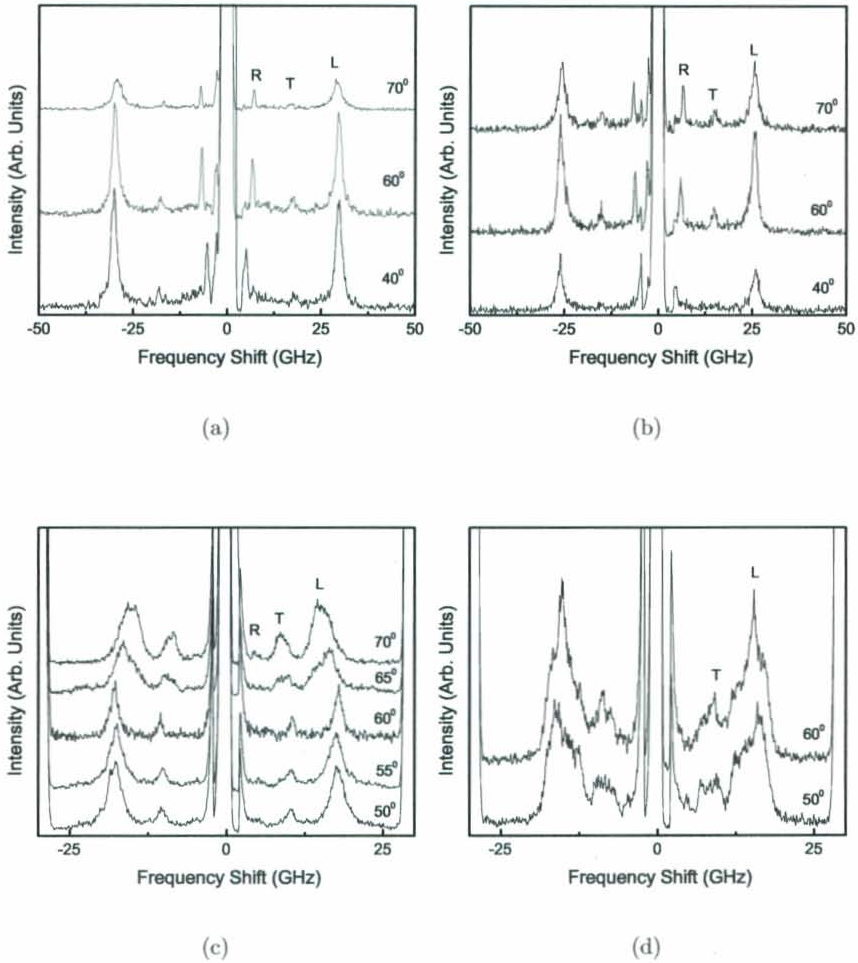

Figure 3.7: Brillouin spectra for a) Sample 3.15#3 with $\xi = 62\%$, b) Sample 3.15#11 with $\xi = 66\%$, c) Sample 3.16#1 with $\xi = 74\%$, and d) Sample 3.16#12 with $\xi = 72\%$.

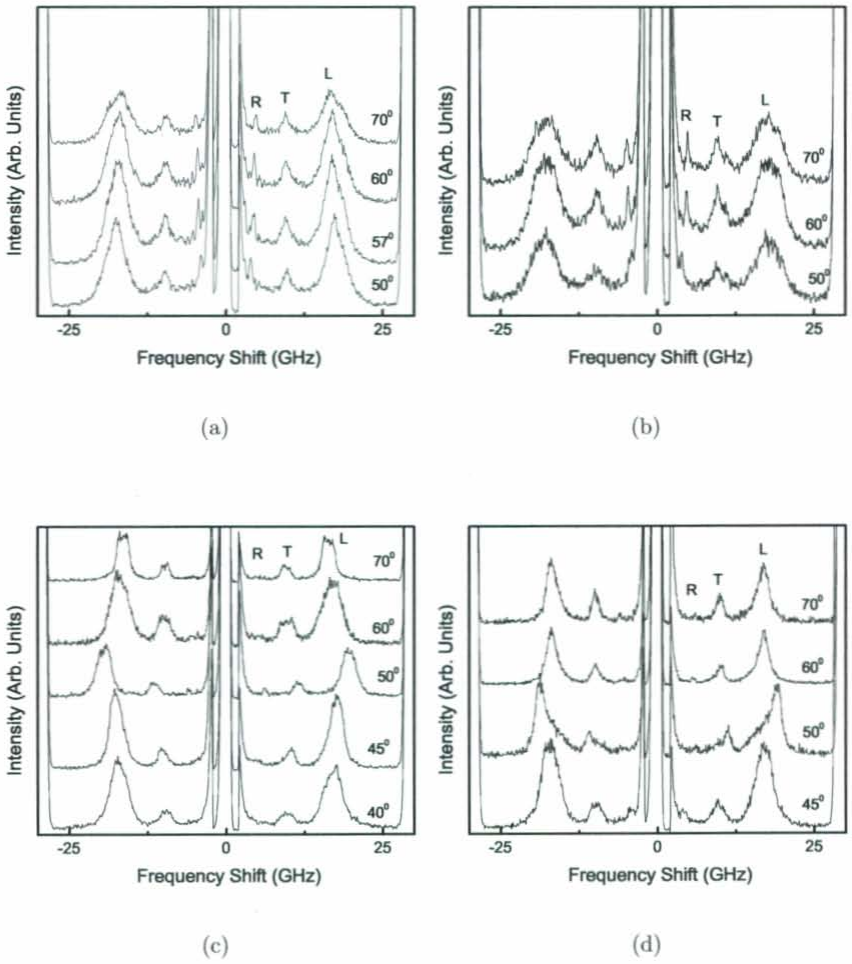

Figure 3.8: Brillouin spectra for a) Sample 5.2#15 with $\xi = 72\%$, b) Sample 5.2#16 with $\xi = 75\%$, c) Sample 3.16#4 with $\xi = 73\%$, and d) Sample 3.16#5 with $\xi = 76\%$.

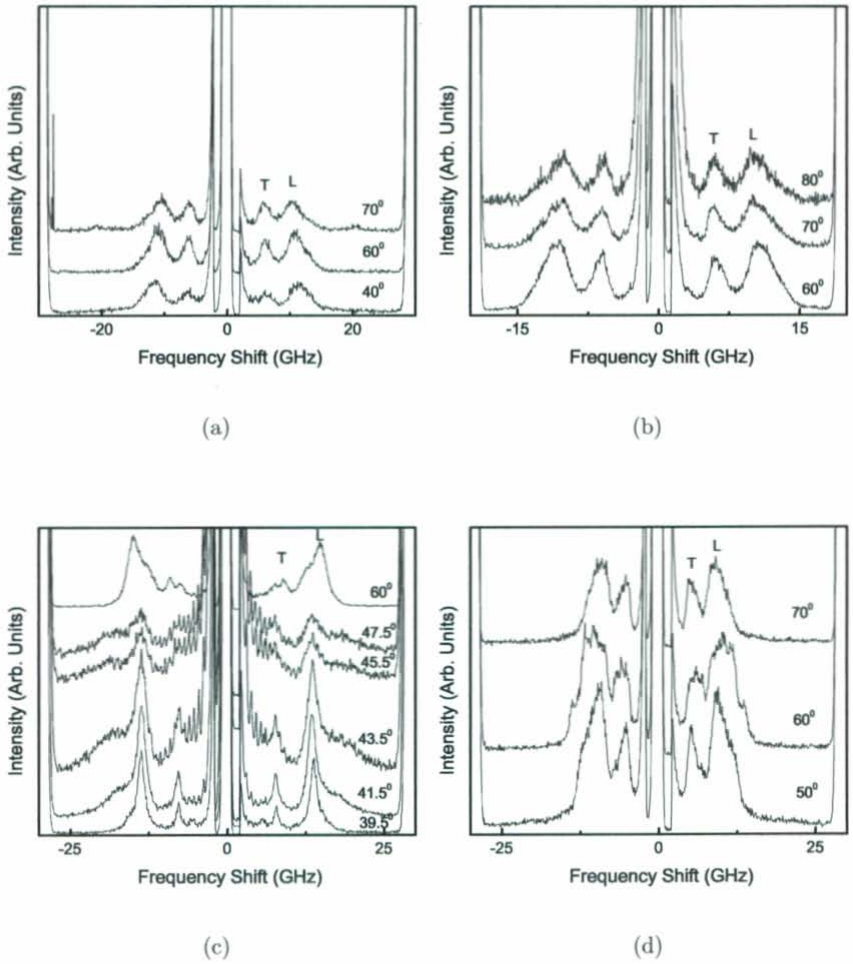

Figure 3.9: Brillouin spectra for a) Sample 3.15#5 with $\xi = 81\%$, b) Sample 3.15#5 @ FSR 20 GHz, c) Sample 3.16#10 with $\xi = 84\%$, and d) Sample 3.16#11 with $\xi = 83\%$.

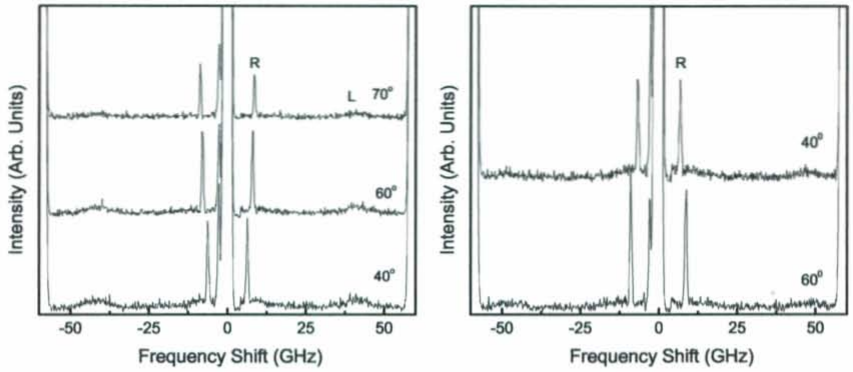

(a) (b)

Figure 3.10: Brillouin spectra for a) Sample 1.17#1 with $\xi = 39\%$, and b) Sample 1.17#2 with $\xi = 50\%$.

Table 3.1: Frequency shifts for sample 3.15#10 determined from Lorentzian fits to Brillouin light scattering data.

θ (^{o}) ($\pm$ 1°)	ν_L (GHz) ($\pm$ 9%)	ν_T (GHz) ($\pm$ 9%)	ν_R (GHz) ($\pm$ 9%)
40	31.16	-	5.22
40	31.15	-	5.19
60	31.03	-	6.80
60	31.01	-	6.69
70	30.73	-	7.18
70	30.73	-	7.13

Table 3.2: Frequency shifts for sample 3.16#8 determined from Lorentzian fits to Brillouin light scattering data.

θ (^{o}) ($\pm 1^o$)	ν_L (GHz) ($\pm$ 9%)	ν_{L2} (GHz) ($\pm$ 9%)	ν_T (GHz) ($\pm$ 9%)	ν_{T2} (GHz) ($\pm$ 9%)	ν_R (GHz) ($\pm$ 9%)
58.5	26.70	-	15.74	-	6.23
58.5	26.61	-	15.59	-	6.16
60	26.55	19.31	15.78	10.48	6.28
60	26.53	19.13	15.77	10.49	6.25
70	26.53	-	15.78	-	6.75
70	26.42	-	15.38	-	6.67

Table 3.3: Frequency shifts for sample 3.16#9 determined from Lorentzian fits to Brillouin light scattering data.

θ (^{o}) ($\pm 1^o$)	ν_L (GHz) ($\pm$ 9%)	ν_T (GHz) ($\pm$ 9%)	ν_R (GHz) ($\pm$ 9%)
50	26.69	15.76	5.67
50	26.78	15.93	5.81
60	26.53	15.42	6.23
60	26.70	15.52	6.41
70	27.43	16.05	6.89
70	27.34	16.05	6.79

Table 3.4: Frequency shifts for sample 3.15#2 determined from Lorentzian fits to Brillouin light scattering data.

θ (^{o}) ($\pm$ 1°)	ν_L (GHz) ($\pm$ 9%)	ν_T (GHz) ($\pm$ 9%)	ν_R (GHz) ($\pm$ 9%)
40	30.06	18.07	5.28
40	29.72	18.04	5.00
60	29.83	17.66	6.77
60	29.70	17.46	6.74
70	29.24	16.93	7.05
70	29.22	16.95	7.09

Table 3.5: Frequency shifts for sample 3.15#3 determined from Lorentzian fits to Brillouin light scattering data.

θ (^{o}) ($\pm$ 1°)	ν_L (GHz) ($\pm$ 9%)	ν_T (GHz) ($\pm$ 9%)	ν_R (GHz) ($\pm$ 9%)
40	30.06	18.07	5.28
40	29.72	18.04	5.00
60	29.83	17.66	6.77
60	29.70	17.46	6.74
70	29.24	16.93	7.05
70	29.22	16.95	7.09

Table 3.6: Frequency shifts for sample 3.15#11 determined from Lorentzian fits to Brillouin light scattering data.

θ (°) (± 1°)	ν_L (GHz) (± 9%)	ν_T (GHz) (± 9%)	ν_R (GHz) (± 9%)
40	26.08	15.53	4.63
40	27.87	15.24	4.67
60	25.95	15.22	6.26
60	25.56	14.84	5.92
70	25.72	15.07	6.62
70	25.58	15.01	6.65

Table 3.7: Frequency shifts for sample 3.16#1 determined from Lorentzian fits to Brillouin light scattering data.

θ (°) (± 1°)	ν_L (GHz) (± 9%)	ν_T (GHz) (± 9%)	ν_R (GHz) (± 9%)
50	17.78	10.34	4.59
50	17.75	10.25	4.90
55	17.57	10.17	5.08
55	17.45	10.21	4.67
60	17.87	10.52	-
60	17.85	10.51	-
65	16.27	9.46	-
65	16.02	9.33	-
70	15.34	8.84	-
70	15.16	8.79	4.44

Table 3.8: Frequency shifts for sample 3.16#1 determined from Lorentzian fits to Brillouin light scattering data.

θ (^{o}) ($\pm$ 1°)	ν_L (GHz) ($\pm$ 9%)	ν_{L2} (GHz) ($\pm$ 9%)	ν_T (GHz) ($\pm$ 9%)	ν_{T2} (GHz) ($\pm$ 9%)	ν_R (GHz) ($\pm$ 9%)
50	16.33	13.38	9.34	6.89	4.67
50	16.34	13.31	9.76	7.09	4.59
60	15.39	12.22	8.89	7.43	-
60	15.61	11.72	8.89	7.05	-

Table 3.9: Frequency shifts for sample 5.2#15 determined from Lorentzian fits to Brillouin light scattering data.

θ (^{o}) ($\pm$ 1°)	ν_L (GHz) ($\pm$ 9%)	ν_T (GHz) ($\pm$ 9%)	ν_R (GHz) ($\pm$ 9%)
50	17.57	9.72	3.92
50	17.42	9.72	3.99
57	17.15	9.66	4.40
57	17.04	9.53	4.31
60	17.10	9.64	4.48
60	17.02	9.59	4.59
70	16.95	9.48	4.78
70	16.91	9.52	4.82

Table 3.10: Frequency shifts for sample 5.2#16 determined from Lorentzian fits to Brillouin light scattering data.

θ (°) (± 1°)	ν_L (GHz) (± 9%)	ν_T (GHz) (± 9%)	ν_R (GHz) (± 9%)
50	17.89	9.78	3.92
50	17.62	9.59	-
60	17.66	9.68	4.67
60	17.63	9.77	4.67
70	17.66	9.74	4.83
70	17.54	9.61	4.85

Table 3.11: Frequency shifts for sample 3.16#4 determined from Lorentzian fits to Brillouin light scattering data.

θ (°) (± 1°)	ν_L (GHz) (± 9%)	ν_{L2} (GHz) (± 9%)	ν_{L3} (GHz) (± 9%)	ν_T (GHz) (± 9%)	ν_{T2} (GHz) (± 9%)	ν_R (GHz) (± 9%)
53	20.37	22.90	-	12.17	-	-
53	20.17	22.79	-	11.91	-	-
54	19.31	-	15.58	11.51	9.14	6.05
54	19.23	-	15.38	11.48	8.81	-
55	19.39	22.61	14.73	11.46	13.73	-
55	19.31	23.36	14.45	11.49	-	-
56	19.89	22.00	-	11.83	13.03	6.39
56	19.91	22.01	-	11.80	13.11	6.34
57	20.63	23.05	15.89	12.19	-	-
57	20.69	22.95	15.67	12.21	-	6.86
40	17.11	-	-	9.60	-	-
40	17.08	-	-	9.71	-	-
60	19.57	-	-	11.52	-	6.18
60	19.39	-	-	11.45	-	6.18

Table 3.12: Frequency shifts for sample 3.16#5 determined from Lorentzian fits to Brillouin light scattering data.

θ (°) (± 1°)	ν_L (GHz) (± 9%)	ν_{L2} (GHz) (± 9%)	ν_T (GHz) (± 9%)	ν_{T2} (GHz) (± 9%)	ν_R (GHz) (± 9%)
45	16.61	17.99	9.67	-	4.09
45	16.79	17.97	9.77	-	4.10
50	16.61	18.77	9.37	10.94	-
50	16.82	19.05	9.53	11.22	-
60	16.88	-	9.87	-	5.26
60	16.92	-	10.04	-	5.61
70	16.85	-	9.89	-	5.78
70	16.83	-	9.94	-	5.72

Table 3.13: Frequency shifts for sample 3.15#5 determined from Lorentzian fits to Brillouin light scattering data.

θ (°) (± 1°)	ν_L (GHz) (± 9%)	ν_T (GHz) (± 9%)	ν_R (GHz) (± 9%)
60	10.89	6.19	-
60	10.89	6.21	-
70	10.51	6.23	-
70	10.38	5.97	-
80	10.34	5.94	-
80	10.33	5.98	-

Table 3.14: Frequency shifts for sample 3.16#10 determined from Lorentzian fits to Brillouin light scattering data.

θ (°) (± 1°)	ν_L (GHz) (± 9%)	ν_{L2} (GHz) (± 9%)	ν_T (GHz) (± 9%)	ν_{T2} (GHz) (± 9%)	ν_R (GHz) (± 9%)
39.5	15.58	13.75	7.77	5.53	-
39.5	15.4	13.74	7.79	5.51	-
41.5	17.09	13.68	7.83	-	-
41.5	16.74	13.4	7.69	-	-
43.5	18.26	13.69	7.63	-	-
43.5	17.81	13.59	7.61	-	-
45.5	19.09	13.78	-	-	-
45.5	18.39	13.53	-	-	-
47.5	18.35	13.77	-	-	-
47.5	18.16	13.55	-	-	-
60	15.02	12.85	7.41	9.13	-
60	14.89	12.66	7.49	9.03	-

Table 3.15: Frequency shifts for sample 3.16#11 determined from Lorentzian fits to Brillouin light scattering data.

θ (°) (± 1°)	ν_L (GHz) (± 9%)	ν_{L2} (GHz) (± 9%)	ν_T (GHz) (± 9%)	ν_{T2} (GHz) (± 9%)	ν_R (GHz) (± 9%)
50	9.43	11.66	5.22	6.79	-
50	9.22	11.24	5.13	6.79	-
60	10.32	-	5.98	-	-
60	10.26	-	6.04	-	-
70	9.36	-	5.56	-	-
70	9.16	-	5.41	-	-

Table 3.16: Frequency shifts for sample 1.17#1 determined from Lorentzian fits to Brillouin light scattering data.

θ (^{o}) ($\pm$ 1°)	ν_L (GHz) ($\pm$ 9%)	ν_T (GHz) ($\pm$ 9%)	ν_R (GHz) ($\pm$ 9%)
40	41.76	-	6.29
40	41.11	-	6.32
60	40.92	-	8.00
60	41.13	-	8.03
70	41.01	-	8.69
70	41.09	-	8.52

Table 3.17: Frequency shifts for sample 1.17#2 determined from Lorentzian fits to Brillouin light scattering data.

θ (^{o}) ($\pm$ 1°)	ν_L (GHz) ($\pm$ 9%)	ν_T (GHz) ($\pm$ 9%)	ν_R (GHz) ($\pm$ 9%)
40	49.69	-	8.96
40	47.89	-	8.63
60	48.55	25.63	6.78
60	46.74	25.33	6.80
70	-	-	-
70	-	-	-

The effect of sample aging on frequency shift was also studied. Figure 3.12 shows the spectra for a sample collected approximately one month apart. It is found that after a month of aging the longitudinal and transverse mode frequency shifts decrease by $\sim$ 2%. A study of natural oxidation is presented in Ref. [35] demonstrated that for longitudinal acoustic modes on p$^-$ type silicon that 21 days after fabrication the frequency shift value decreased approximately 6 GHz. This oxidation process

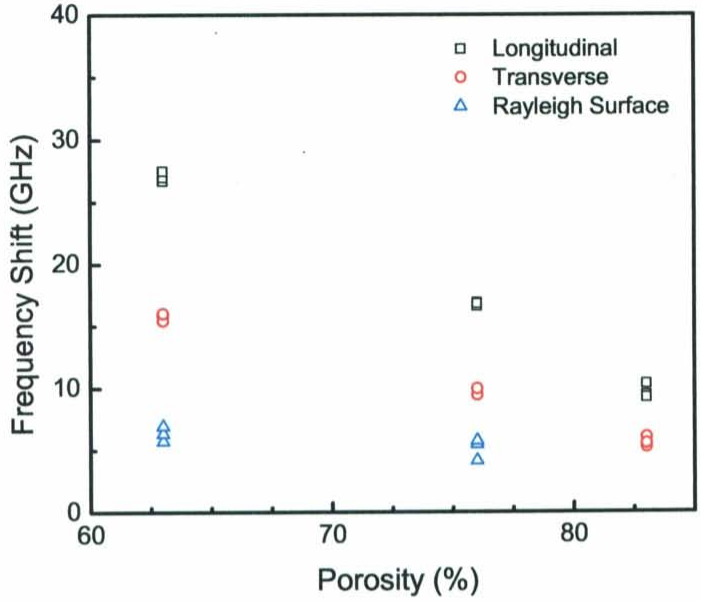

Figure 3.11: Frequency shift values determined from Brillouin light scattering spectra as a function of porosity plotted for a 63%, 76% and 83% sample.

transforms the pore walls into SiO_2, which eventually, if completely oxidized, leads to a form of porous glass [35]. Fan *et al.* also demonstrated that after a period of 7-10 days the effect of the natural oxidation on the frequency shift value is negligible [35]. In this work, samples were allowed to age for at least 10 days before BLS. Further, spectra of different angles of incidence per sample were collected consecutively to minimize any effects of natural oxidation.

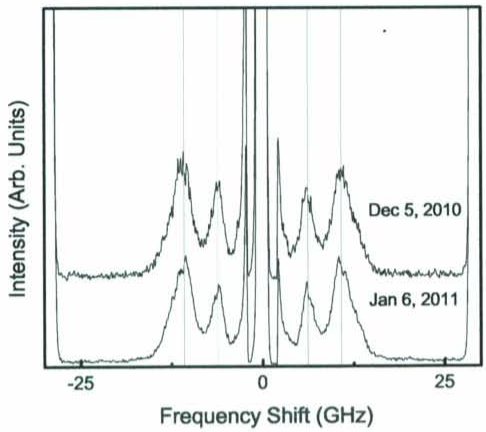

Figure 3.12: Comparison of Brillouin spectra for sample 3.15#5 after fabrication and after 30 days aging in ambient air.

3.3.2 Phonon Velocities

The phonon velocities of micro- and mesoporous silicon films are presented in Table 3.18. To determine the velocity corresponding to the Rayleigh surface mode, the values of frequency shift were plotted as a function of $\sin\theta$ and fit to Equation (3.13). To determine bulk mode velocities the frequency shifts corresponding to each mode were averaged. The phonon velocity was then determined using Equation (3.14). In cases where a frequency shift value could not be determined for the Rayleigh or transverse acoustic mode, Viktorov's relation,

$$v_R = v_T \cdot \frac{0.72 - (v_T/v_L)^2}{0.75 - (v_T/v_L)^2}, \tag{3.36}$$

was used to find the velocity [75]. The velocities for each peak are displayed in Table 3.18.

Figure 3.13 shows the Rayleigh surface mode velocity as a function of porosity, as well as data collected for other porous silicon samples fabricated on p^- type samples given in Refs. [23] and [38]. It can be seen that in general, as porosity increases the surface mode velocity decreases. The same overall trend is displayed in the data collected by Fan *et al.* [23]. However, in the porosity range of 55% to 65 % there is a disagreement between the current data and that collected by Fan in that the velocities reported are approximately 30% larger. This can be attributed to the fact that the lowest porosity samples reported by Fan are fabricated on substrate with resistivity of 0.005 Ω·cm. These velocities however do agree with velocities reported for samples fabricated on similar resistivity bulk silicon with similar pore morphology [30,33,37]. Andrews *et al.* demonstrated that the Rayleigh surface wave velocities for samples formed on substrates with resistivity 0.02 Ω·cm agreed with velocities for higher resistivity samples ($\rho > 0.1$ Ω·cm) [37]. The difference in phonon velocities for films fabricated from high and low resistivity silicon is due to the difference in the resultant pore morphology for the same porosity. The higher resistivity samples have a more random and interconnected pore structure, with pore diameters of 1 - 5 nm, versus lower resistivity samples which yield highly directional pores with sizes of 10 - 15 nm [8, 22]. Also, p^- type porous silicon incorporates 9 times more oxygen into its structure when exposed to air [76], which has been shown to reduce the Rayleigh

Table 3.18: Phonon velocities determined from Brillouin light scattering data. ([1]:calculated using Equation (3.36))

Sample	ξ ($\pm$ 0.02)	n ($\pm$ 4%)	v_L (km/s) ($\pm$ 5%)	v_T (km/s) ($\pm$ 5%)	v_R (km/s) ($\pm$ 5%)
3.15#10	0.59	2.10	3.9	2.6 [1]	1.77
3.16#8	0.65	1.88	3.8	2.2	1.59
3.16#9	0.63	1.92	3.7	2.2	1.96
3.15#2	0.59	2.14	3.7	2.2	1.78
3.15#3	0.62	2.00	3.5	2.0	1.89
3.15#11	0.66	1.84	3.8	2.2	1.76
3.16#1	0.74	1.54	2.9	1.70	1.61
3.16#12	0.72	1.61	2.6	1.50	1.40
5.2#15	0.72	1.60	2.9	1.60	0.87
5.2#16	0.75	1.51	3.1	1.71	1.36
3.16#4	0.73	1.57	3.8	1.94	1.81 [1]
3.16#5	0.76	1.48	3.0	1.75	1.95
3.15#5	0.81	1.35	2.1	1.20	1.11 [1]
3.16#10	0.84	1.28	2.8	1.59	1.47 [1]
3.16#11	0.83	1.29	2.0	1.15	1.06 [1]
(n^+) 1.17#1	0.39	2.90	3.8	2.24[1]	2.05
(n^+) 1.17#2	0.50	2.47	5.2	2.74	2.40

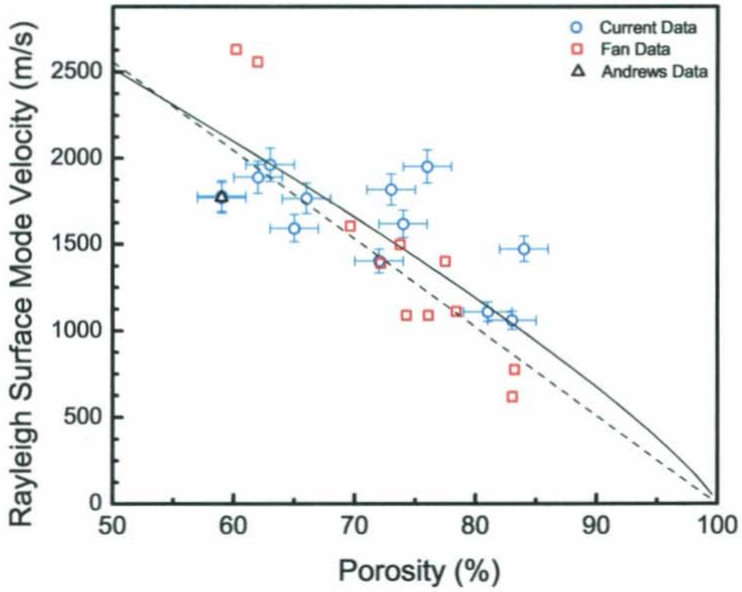

Figure 3.13: Rayleigh surface mode velocities calculated from Brillouin light scattering spectra (Blue points), and data from Ref. [23] (Red points). Dashed lines correspond to fit with $v = v_o(1-\xi)^m$ where for $m = 1.004$, and $v_o = 5130$ m/s. Solid line is a fit with $v_o = 4445$ m/s giving m = 0.820.

surface mode velocity [35, 77].

Figure 3.14 displays the experimental transverse and longitudinal mode velocities, along with previously reported data [23,38]. General inspection shows that as porosity increases the bulk mode velocity decreases. This trend agrees with previous reports in Ref. [23] for p^- samples and Refs. [30, 33] for p^+ samples.

It has been shown that the relationship between velocity and porosity can be described by the relation

$$v = v_o(1-\xi)^m \tag{3.37}$$

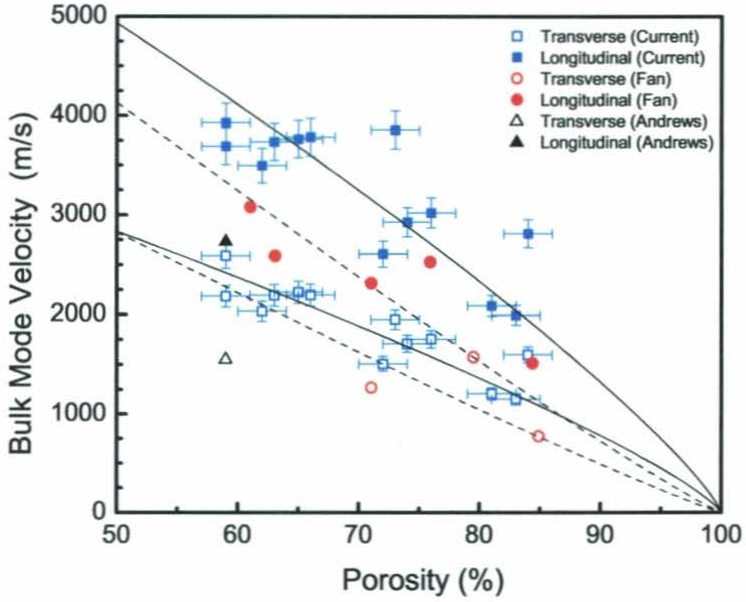

Figure 3.14: Bulk mode velocities calculated from Brillouin light scattering spectra (Blue points), and data from Ref. [23] (Red points). Dashed lines correspond to fits with $v = v_o(1-\xi)^m$ where for transverse and longitudinal respectively, m is 1.086 and 1.083, and v_o is 6000 and 8750 m/s [23]. Solid lines corresponds to fits of the equation to the experimental data with v_o set to 4940 and 8700 m/s giving m 0.801 and 0.819 for the transverse and longitudinal data respectively.

where v_o is the velocity of the corresponding mode in bulk Si and m is an empirical parameter, shown to be dependent on the microstructural details of the porous material [23, 78]. In Figure 3.13 the solid curve is a fitted line to the experimental data collected in this work with $v_o = 4445\ m/s$ (the Rayleigh surface mode velocity determined from BLS on a piece of crystalline silicon) resulting in a value of $m = 0.820$. The dashed curve represents Equation (3.37) for the value of m reported in [23] of 1.004 (Rayleigh) with v_o set to the value for bulk silicon. Table 3.19 presents the

values collected in this work along with values previously determined using the same method for different bulk silicon resistivity than used in this work.

Similarly, in Figure 3.14 the solid curves are fits of $v = v_o(1 - \xi)^m$ to the experimental data collected in this work with v_o set to 4940 m/s, and 8700 m/s for the transverse, and longitudinal modes respectively. The m values from these fits were determined to be 0.801 and 0.819, respectively. The dashed curves represent Equation (3.37) using m values reported by Fan *et al.* of 1.086 for the transverse and, 1.083 for the longitudinal and v_o values of bulk silicon [23].

It was shown by Phani *et al.* that for a relatively ordered and less open pore structure, $0.5 < m < 1.5$, and for higher values of the m a more disordered and interconnected structure is found [30, 34, 78]. Fan *et al.* concluded that the samples presented in their work displayed a relatively ordered and less-open pore structure based on the value of m from the fit of Equation (3.37) [23]. Lockwood *et al.* concluded the same from a fit of Rayleigh surface velocities, agreeing with TEM and Raman analyses [34, 79, 80]. Based on the results of the fits to the data in this work, the samples have a more ordered, and less open pore structure, agreeing with those formed on p^- bulk substrate by Fan [23] and Lockwood [34]. In comparison, fitting of Equation 3.37 to velocities reported for mesoporous data gave values (Longitudinal $m = 0.73$ and 0.58 [81], Transverse $m = 0.89$ [64]) lower compared to values determined for microporous silicon samples. It has previously been demonstrated that for higher values of m, within the range of 0.5 - 1.5, the pore structure is more

Table 3.19: Comparison of values for m for fits of $v = v_o(1-\xi)^m$ to the phonon velocities.

		Current data	Fan [23]	Lockwood [34]	da Fonseca [30]
Rayleigh	m	0.820	1.004	0.84	-
	v_o	4445	5130	-	-
Transverse	m	0.801	1.086	-	-
	v_o	4940	6000	-	-
Longitudinal	m	0.819	1.083	0.72	1.095
	v_o	8700	8750	8570	8570

disordered [30, 78]. This is expected as in general for these samples it is well known that as the bulk silicon resistivity is decreased the pore size and interpore spacing increases and the resultant morphology becomes more ordered and columnar for B-doped silicon as used in this work [8, 12]. It is notable that fits were also done for Equation (3.37) with v_o allowed to vary during the fit, resulting in $m = 0.493$ and $v_o = 2912$ m/s for the Rayleigh surface velocity, $m = 0.698$ and $v_o = 4309$ m/s for the transverse velocity and $m = 0.641$ and $v_o = 6888$ m/s for the longitudinal velocities. Obviously the fit value found for the bulk silicon velocity is much smaller than those found by employing BLS on a piece of crystalline silicon (4445 m/s, 4940 m/s, and 8700 m/s for the Rayleigh surface, transverse, and longitudinal modes respectively.) In terms of use as a tissue engineering scaffold, an open pore structure is ideal as it promotes three-dimensional healing as well as growth of cells [82, 83].

3.3.3 Elastic Constants

The elastic constants of microporous samples are reported here for porosity values between 59% and 84% fabricated on p^- type silicon for the first time. Also, the elastic constants of mesoporous silicon samples formed on n^+ type silicon are calculated for comparison with Young's Modulus values determined by nanoindentation techniques.

The elastic constants of the porous silicon films were calculated using Equations (3.29) and (3.30), as well as the relation for isotropic media, $C_{12} = C_{11} - 2C_{44}$. The resultant elastic constants, given in Table 3.20, are plotted as a function of porosity in Figure 3.15 showing that as porosity is increased, C_{11}, C_{12}, and C_{44} decrease. This corresponds to what has been demonstrated in Refs. [5, 23, 31, 64] for p-type porous silicon samples formed on different resistivity substrates than in this work. Overall, the excellent agreement of the individual data points to the general trend corroborates the assignment of the longitudinal and transverse modes. The overall trend displayed by the elastic constants also agrees with theoretical studies of porous silicon reported by Al-Douri *et al.* with porosities in the range 27% - 88% [84].

The elastic constants calculated for samples with similar porosity values show excellent agreement. The only exception to the previous statement is found in the 72% - 76% range. The values of C_{11} and C_{12} for sample 3.16#4 are much higher than other samples in this porosity range. This may be due to the assignment of the longitudinal peak. In Figure 3.8c, doublet longitudinal peaks are present in the BLS data. The assignment of frequency shift was done for the peak appearing in spectra

for each angle. However, if instead the second peak of the doublet (ν_{L2} = 15.289 GHz) a value of C_{11} of 4.22 GPa is found, which is in much better agreement with the values in Table 3.20 for similar porosity. Further work is required on these doublets before a conclusion can be made.

The agreement between the data presented in this work and data from Fan *et al.* is especially obvious for C_{12} and C_{44} in Figure 3.15. In comparison with values presented by Andrews *et al.*, values of C_{11}, C_{12} and C_{44} do not fall within the error for the 59% samples in this work. The reason for this difference is unknown.

In comparison to values of the elastic constants calculated for p^+ type samples, shown to have cubic symmetry, the values reported here are lower. Andrews *et al.* reported values of C_{11}, C_{12} and C_{44} for a 30% porous sample to be 56.0 GPa, 6.7 GPa, and 37.0 GPa, respectively. These values are between 31% - 97% larger than those reported here for microporous silicon [36]. Similarly, a 62% porous sample fabricated on p^+ type bulk silicon with cubic symmetry yielded C_{11}, C_{12} and C_{44} of 18.2 GPa, 5.5 GPa, and 5.0 GPa, respectively [14]. In comparison to the 62% porous sample (3.15#3) present in Table 3.20, the values of C_{11}, C_{12} and C_{44} presented by Polomska *et al.* are 1.7, 3.7, and 1.4 times larger, respectively. Similarly, Andrews *et al.* compared values of C_{11} and C_{12} for 60% micro- and mesoporous films, reporting that mesoporous sample values were 2.76 and 2.89 times larger respectively [38].

The Young's modulus and the bulk modulus were calculated from the elastic constants using Equations (3.31) and (3.32), respectively. The resultant data is given

Table 3.20: Elastic constants, and Young's Modulus determined from Brillouin light scattering data.

Sample	ξ ($\pm$ 0.02)	C_{11} (GPa) ($\pm$ 10%)	C_{12} (GPa) ($\pm$ 20%)	C_{44} (GPa) ($\pm$ 10%)	E (GPa)	B (GPa)
3.15#10	0.59	15.0	3.7	7.7	9.8	7.5
3.16#8	0.65	11.5	3.5	4.0	9.9	6.2
3.16#9	0.63	11.7	3.6	4.0	9.9	6.3
3.15#2	0.59	13.0	4.6	3.9	11.2	7.4
3.15#3	0.62	10.9	1.5	3.7	9.2	4.6
3.15#11	0.66	11.4	3.8	3.7	9.6	6.3
3.16#1	0.74	5.2	1.7	1.8	4.4	2.9
3.16#12	0.72	4.5	1.5	1.5	3.8	2.5
5.2#15	0.72	5.3	2.0	1.7	4.2	3.1
5.2#16	0.75	5.6	2.2	1.7	4.4	3.3
3.16#4	0.73	9.3	4.6	2.4	6.3	6.2
3.16#5	0.76	5.1	1.7	1.7	4.3	2.8
3.15#5	0.81	2.0	0.7	0.6	1.6	1.1
3.16#10	0.84	2.9	1.1	0.9	2.4	1.7
3.16#11	0.83	1.6	0.5	0.5	1.3	0.9
(n^+) 1.17#1	0.39	20.1	5.7	7.2	17.6	10.5
(n^+) 1.17#2	0.50	31.4	13.9	8.8	22.9	19.7

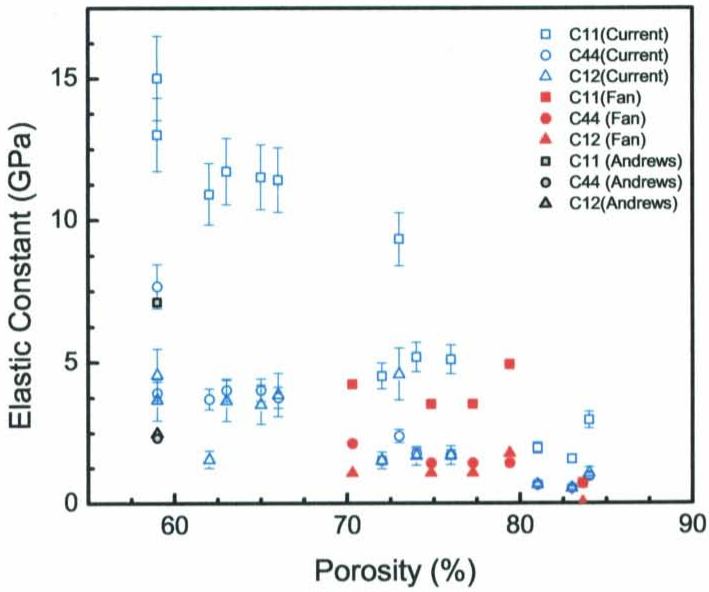

Figure 3.15: Elastic Constants as a function of porosity for p^- type samples.

in Table 3.20, and is plotted as a function of porosity in Figures 3.16 and 3.17. It can be seen that as the porosity of the porous silicon film is increased, both Young's modulus and the bulk modulus decrease. For the purpose of direct comparison, samples on bulk silicon with resistivity of 2.5 - 4.0 Ω·cm (3.16#1 / 3.16#12) and ρ = 9.0 - 13.0 Ω·cm (5.2#15 / 5.2#16) were fabricated under conditions as reported by Bellet *et al.* [31] (I = 28 mA, 1 HF : 1 C_2H_5OH). Bellet determined that samples fabricated under the previously mentioned conditions on 5 Ω·cm bulk silicon had E = 2.4 GPa through nanoindentation experiments. The samples fabricated under these conditions in this work were determined to have Young's modulus values in the range

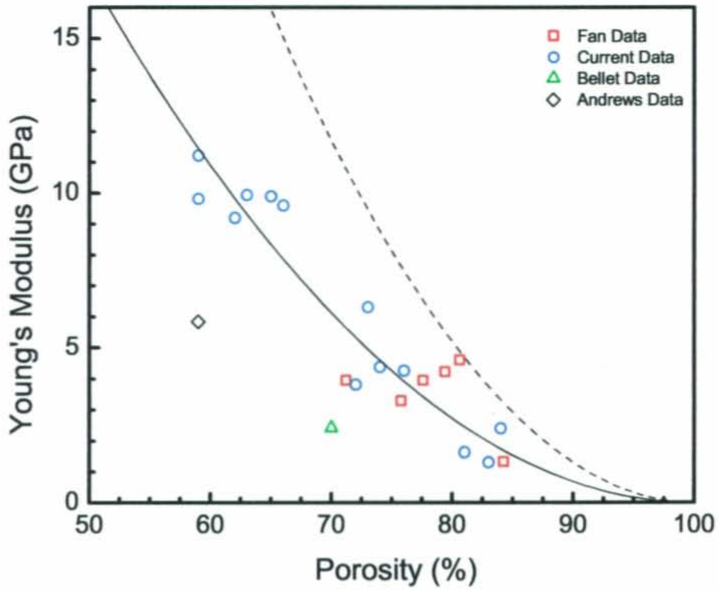

Figure 3.16: Young's modulus as a function of porosity for p^- type samples. Dashed line represents a simulation of Gibson Ashby relation for $E_B = 130$ GPa corresponding to bulk silicon. Solid line represents a fit of the Gibson Ashby relation giving $E_B = 68$ GPa.

of 3.8 - 4.4 GPa, almost twice as large as the value reported in [31].

One can also see from Table 3.20 that the elastic constants and Young' modulus for n^+ type samples are much higher than those made on p^- type samples (not included in the Figures 3.15, 3.16 or, 3.17). It is important to note that these values for the n-type samples assumes that the films are isotropic. A comparison for samples of the same porosity cannot be made as no samples were fabricated to enable this in this work. However, a n^+ type sample with a porosity of 50% has a Young's modulus value 2.4 times larger than a p^- type sample with a porosity of 59%, which

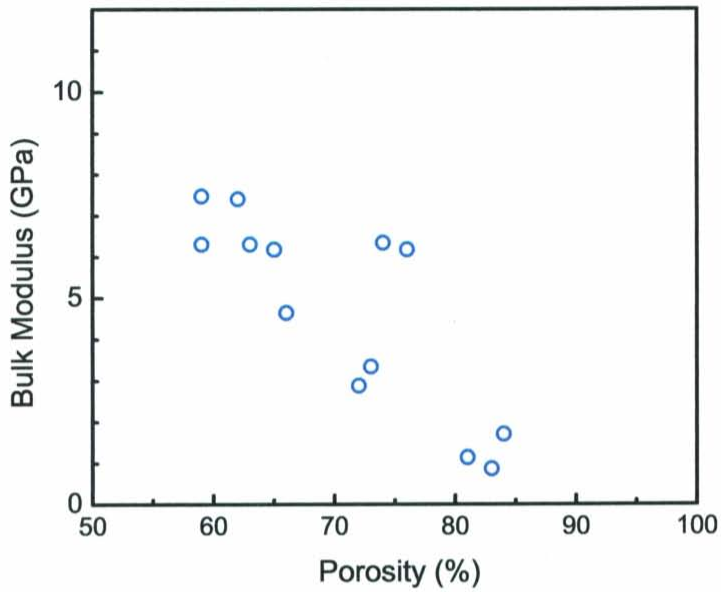

Figure 3.17: Bulk modulus as a function of porosity for p^- type samples.

can be at least partially attributed to the difference in the resultant pore structure and morphology. Previously, it has been shown that the Young's modulus calculated by nanoindentation on p^- and p^+ porous silicon for samples of 70% porosity yield very different results, 2.4 GPa and 12.0 GPa, respectively [31]. Andrews *et al.* have shown that the ratio of Young's Modulus between a p^+ sample and a p^- sample with approximately the same porosity was 2.71 [38]. Comparing the n^+ sample from this work to the p^+ sample in [38], the Young's modulus ratio is 1.4.

The Gibson-Ashby relation for open pore foam structures was fitted to the data in Figure 3.16 [85]. This relation considers that an open-cell foam can be modeled

as a cubic array of members of the same length and cross section, and the adjoined members stagger such that the members meet at their midpoint [31]. The Young's modulus is calculated from the linear-elastic deflection of a member loaded at the midpoint through standard beam theory which leads to

$$E = CE_B\rho_r^2 \tag{3.38}$$

where ρ_r is the relative density ($\rho_r = 1-\xi$), E_B is the Young's modulus of bulk silicon, and C is a constant term containing all of the geometric constants of proportionality [85]. It is known that C is on the order of unity through comparison with data obtained from rigid polymers, elastomers, metals, and glasses of a wide density range [31, 85]. The dashed line represents the Gibson Ashby relation for $E_B = 130$ GPa which is the Young's modulus of [100]-oriented bulk silicon [8]. The solid line is a fit of the Gibson Ashby relation with $C = 1$, resulting in $E_B = 68$ GPa, much smaller than the expected value for bulk silicon. In Ref. [31], Equation (3.38) was fit to Young's modulus values calculated by nanoindentation techniques of p^+ type samples finding E_B=120 GPa, in good agreement with the expected value of E_B (162 GPa for p^+ type silicon). This agreement can be attributed to the fact that p^+ type samples exhibit an open pore, tri-dimensional arrangement corresponding to the Gibson-Ashby model [31]. The difference in E_B value determined in this study may be due to the fact that requirements of the Gibson and Ashby relation are not fulfilled by the small and complicated pore morphology of the p^- type silicon used here [31].

Andrews [86] demonstrated through the comparison of p^+ type samples with [100]- and [111]-crystal orientation that a significant difference in Young's modulus is found. Therefore, the influence of the elastic anisotropy on the Young's modulus must be taken into account for p^+ type samples. For comparison purposes, the solid line can also represent a fit of Equation (3.38) to the data in this work with $E_B = 130$ GPa, allowing C to vary resulting in $C = 0.52$. The large difference between the value of C from the fit and the value expected of unity shows that this relation does not apply to p^- type porous silicon. It has previously been shown that in the case of closed cell foams some variations in the C term occur possibly due to variable geometry of the foams or a fraction of solid in the cell faces [85]. This result agrees with the less open of pore structure of microporous silicon films discussed in Sec. 3.3.2, which aids in the candidacy of porous silicon as a tissue engineering scaffold.

Overall it is demonstrated that these porous silicon films can be fabricated with a wide range of elastic constants. In the case of bone tissue engineering the elastic moduli must be tailored for the specific application such that the mechanical properties can withstand physiological stresses [82].

Chapter 4

Bioactivity of Porous Silicon

Understanding the factors influencing the bioactivity of porous silicon films is necessary for biomaterial applications. Many proposed scaffolds in tissue engineering have limited efficacy as they do not take biological aspects into consideration, which become increasingly significant with the goal of tissue integration into the scaffold [82]. The degradation of porous silicon films in simulated body fluid is known to release the non-toxic aqueous form of silicon, orthosilic acid. Limited work has been done on the rate at which these films degrade and release silicon. In this chapter, the dissolution rate of micro-, meso-, and macroporous silicon films measured in simulated body fluid are given. It is demonstrated that the dissolution rate of porous films can be predicted with knowledge of the nonporous bulk material dissolution rate, and the films thickness and specific surface area. The bioactivity in simulated body fluid of macroporous silicon films is also presented. Using scanning electron microscopy and

energy dispersive x-ray techniques it is shown that calcium phosphate was deposited on the surface of the porous silicon films.

4.1 Experimental Setup

Simulated body fluid (SBF) was mixed based on the recipe by Kokubo *et al.* presented in Ref. [42]. The ion concentrations in SBF are given in Table 4.1 along with the ion concentrations in blood plasma for comparison. The actual reagents required, as well as the required masses of each are given in Table 4.2.

For dissolution experiments, the fabrication conditions for the micro-, meso-, and macroporous silicon samples are given in Table 4.3. The mesoporous and macroporous samples were first oxidized by soaking in H_2O_2 for 24 hours. Microporous samples were left to naturally oxidize in ambient air for the same amount of time because microporous samples immersed in H_2O_2 crumbled when removed from the solution. Following oxidation, the porous silicon films were immersed in the SBF in cleaned and sterilized glass petri dishes. The dissolution of the porous silicon samples was measured by removing the samples after timed intervals of approximately 8 hours and weighing. When removed from SBF for weighing, the samples were subject to sequential dips in baths of tap water, then rinsed in a stream of nanopure water to remove any material on the surface. Samples were padded dry using paper towel to remove excess water and then left covered in ambient air for 15 minutes. It is notable that possible errors due to remianing liquid in the pores or material on the surface

have not been accounted for in the measurements. Mass measurements were done using a Sartorius CP 225 D analytical balance. Before being placed back into SBF, pH readings of the SBF were taken and compared to SBF in a petri dish with no π-Si to ensure that no change in pH occurred. Maintaining a constant pH is important as it has been shown that a slight decrease in pH value from 7.4 to 8 can greatly increase the dissolution rate [45].

Energy dispersive X-ray (EDX) spectra were collected using a high speed, high resolution Roentec Quantax EDX system with the Xflash SDD detector installed on an FEI Quanta 400 environmental scanning electron microscope (SEM). The EDX spectra were analyzed using simple graphical analysis programs (Corel Paint Shop Pro Photo X2).

4.2 Results and Discussion

4.2.1 Dissolution

Plots of the dissolution rates of the porous silicon films are displayed in Figure 4.1 for microporous, mesoporous, and macroporous samples. The dissolution rates, presented in Table 4.4, were determined by fitting the mass loss of the samples to linear equations using graphical analysis software. It is notable that in microporous silicon plot in Figure 4.1, the linear fits were not applied to the data for which no porous layer was left to dissolve. This time was determined through comparison of estimates of the

Table 4.1: Ion concentrations in human blood plasma compared to ion concentrations in simulated body fluid.

Ion	Blood Plasma (mmol/dm^3)	SBF (mmol/dm^3)
Na^+	142.0	142.0
K^+	5.0	5.0
Mg^{2+}	1.5	1.5
Ca^{2+}	2.5	2.5
Cl^-	103.0	103.0
HCO_3^+	27.0	10.0
HPO_4^{2-}	1.0	1.0
SO_4^{2-}	0.5	0.5

Table 4.2: Reagents for the preparation of simulated body fluid.

Order	Reagent	Amount
1	$NaCl$	7.996 g
2	$NaHCO_3$	0.350 g
3	KCl	0.224 g
4	$K_2HPO_4{\cdot}3H_2O$	0.228 g
5	$MgCl_2{\cdot}6H_2O$	0.305 g
6	HCl	40 cm^3
7	$CaCl_2$	0.278 g
8	Na_2SO_4	0.071 g
9	$(CH_2OH)_3CNH_2$	6.057 g
10	HCl	–

Table 4.3: Fabrication parameters and porosity for micro-, meso- and macroporous silicon films used for dissolution.

Type	Resistivity (Ω·cm)	Current (mA)	Time (s)	Electrolyte Composition	Porosity (%)
Micro	9.0 - 13.0	15	1750	1 49% HF : 1 C_2H_5OH	65
Micro	2.5 - 4.0	15	1750	1 49% HF : 1 C_2H_5OH	75
Micro	2.5 - 4.0	10	1900	2 49% HF : 3 C_2H_5OH	85
Meso	0.005 - 0.020	135	145	1 49% HF : 1 C_2H_5OH	50
Meso	0.005 - 0.020	300	90	1 49% HF : 1 C_2H_5OH	70
Macro	9.0-13.0	14	600	1 49% HF : 14 CH_3CN	-

sample mass with no porous layer remaining to the weighed mass of the sample. It can be seen in Figure 4.1 that in this area the slope is approximately zero.

For the microporous samples it can be seen in Figure 4.1 that the dissolution rate for the 65% porosity sample is higher than that of the 75% porous samples and both are much higher than that of the 85% porous sample. For microporous silicon films on p^- type bulk it has been shown that the specific surface area reaches a maximum of around 1000 m^2/cm^3 for a 50% porous sample [87]. These dissolution rates then can be attributed to the difference in the total surface area of each sample. It can be estimated by extrapolation of the results presented in Ref. [87] that, from low to high porosity, the samples shown in Figure 4.1 had a specific surface area of approximately 725 m^2/cm^3, 600 m^2/cm^3, and 375 m^2/cm^3 respectively. Since the specific surface area of the 65% and 75% porous samples differ by only 20%, whereas the specific surface area of 65% and 85% samples differs by 50%, it is understandable that the dissolution rates would be more similar for the 65% and 75% and greatly reduced for

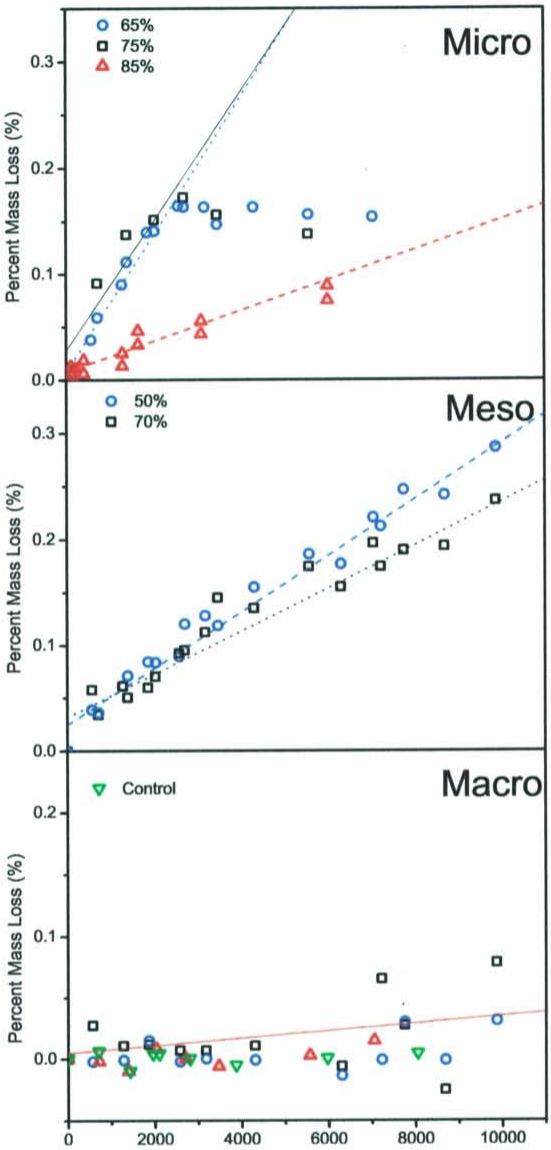

Figure 4.1: Dissolution of microporous, mesoporous, and macroporous silicon samples in SBF. In the microporous plot the dotted line corresponds to a linear fit to data for a 65% porous film, solid line corresponds to a linear fit to data for a 75% porous film, and dashed line corresponds to a linear fit to data for a 85% porous film. In the mesoporous plot the dashed line corresponds to a linear fit to data for a 50% porous film, and the dotted line corresponds to a linear fit to data for a 70% porous film.

Table 4.4: Dissolution rates for samples in SBF determined by a linear fit to the data.

Type	Porosity (%)	Dissolution Rate [$\times 10^{-5}$] (%·min^{-1})
Micro	65	6.47
Micro	75	6.08
Micro	85	1.44
Meso	50	2.66
Meso	70	2.04

the 85% porous sample.

For the mesoporous samples, shown in Figure 4.1, the difference in the dissolution rates for the 50% and 70% porous samples is not as large as seen for the microporous films with similar porosity. The pre-dissolution specific surface area of the samples is approximately 230 m^2/cm^3 and 190 m^2/cm^3, respectively [88]. In a study done by Anderson *et al.* on the behavior of mesoporous silicon films in buffered solutions, it was demonstrated that for the higher porosity films, 83% and 88%, the mass loss was exponential with time, while the lower porosity sample, 62%, showed negligible silicon release over a 24 hour period, reported to be approximately 7% of the original mass [45]. In this study, in the first 24 hours a similar mass loss for both the 50% and 70% samples is found. However, it is notable that overall the 50% mesoporous sample does have a higher dissolution rate than the 70% sample, which is expected due to the larger specific surface area of the 50% sample.

Another interesting comparison to make is the dissolution of the micro- and mesoporous films. Since the specific surface area of the microporous samples is much higher

than the mesoporous samples of the same porosity due to is smaller pore size and random interconnected morphology, it is expected that the dissolution rate for microporous samples as compared to mesoporous samples of similar porosity would be higher. Comparing the 75% microporous sample with the 70% mesoporous sample, the dissolution rates of the microporous sample is almost three times larger. Comparing the surface area of these two samples it is notable that the surface area of the microporous is more than three times larger than that of the mesoporous sample. In comparison, the 85% microporous sample and the 70% mesoporous samples have similar dissolution rates, for which it is notable that both have similar surface areas. If then total surface area is the main factor in sample dissolution in SBF, following the discussion in [87] for chemical etch rates of porous silicon samples in hydrofluoric acid, the equation

$$\frac{dM}{dt} = \Lambda \cdot SA \cdot d \tag{4.1}$$

can be adapted where $\frac{dM}{dt}$ is the rate of change of the mass of the film, Λ is the rate of mass loss of bulk silicon in SBF determined to be approximately 3×10^{-11} g·min^{-1} by monitoring the mass of crystalline silicon in SBF (see Figure 4.2), SA is the specific surface area of the sample, and d is the sample thickness (here $d \simeq 15$ μm). This equation allows prediction of the dissolution rate in SBF . The values obtained from fits of the data are compared to the values calculated using Equation (4.1) in Table 4.5. As can be seen, Equation (4.1) provides a very good estimate of the dissolution

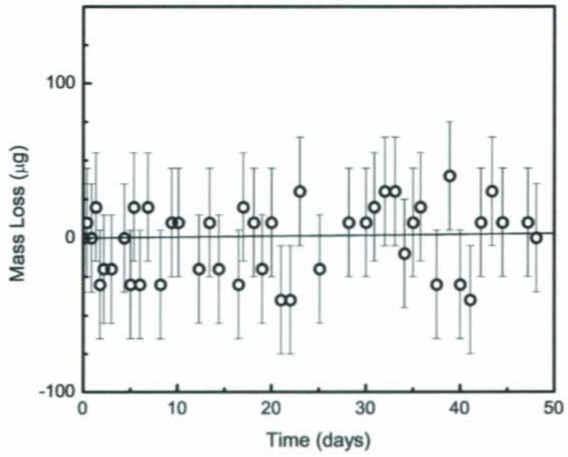

Figure 4.2: Dissolution rate of crystalline silicon in SBF. Fit resulted in a dissolution rate of 0.06 ± 0.13 μg·min^{-1}.

rate with the exception of the 85% microporous sample which resulted in a difference of over 50%. The reason for this large difference is unknown, but may be due to the surface of the film being etched away during fabrication.

Finally, the dissolution of the macroporous samples in SBF was shown to occur at a similar rate as the control sample of bulk silicon (see Figure 4.1). This is expected as the larger pore diameter and columnar pores will not increase the surface area to the degree seen for microporous and mesoporous samples. If macroporous silicon is estimated to have a specific surface area of $\sim$10 m^2/cm^3, then Equation (4.1) predicts that the rate of mass loss will be approximately 4.5 ng·min^{-1}, about 75 times smaller than for a 65% microporous film. This result for macroporous samples is promising seeing that it can take days to weeks for deposition of hydroxyapatite on silicon films

Table 4.5: Comparison of the dissolution of silicon per minute of the micro- and mesoporous samples.

	Porosity (%)	Experimental (μg·min^{-1})	$\Lambda \cdot SA \cdot d$ (μg·min^{-1})	% difference
Micro	65	0.36	0.33	10
Micro	75	0.30	0.27	10
Micro	85	0.08	0.17	52
Meso	50	0.12	0.10	14
Meso	70	0.09	0.09	8

immersed in SBF [49]. Further, it has been shown that as a cell growth medium, macroporous silicon promoted osteoblast growth and maturation, with calcification in the bone growth process much faster than microporous or mesoporous silicon [27].

4.2.2 Hydroxyapatite Deposition

Coatings of hydroxyapatite on porous silicon films could potentially improve their biomaterial properties. Moreover, no reports of the bioactivity in SBF of p^- type macroporous silicon films are available, despite these films having been shown to out perform micro- and mesoporous silicon films as a growth medium for osteoblast cells, the cell responsible for mineralization of bone during initial formation [27, 54].

Macroporous silicon samples, oxidized in H_2O_2 for 24 hours, were immersed in SBF heated to 37°C for periods of up to 45 days. Figure 4.3a shows a cross sectioned SEM micrograph of a macroporous sample with a deposit in the pores. Figure 4.3b shows an SEM image of the surface of a porous silicon film with HA spherules on

the surface. As seen here, HA deposits previously observed are small spherules with a characteristic average diameter size of about 100 nm [50]. These SEM images are similar to those presented in several previous studies on porous silicon films [4, 39, 40, 48, 50, 51, 53, 89, 90].

To demonstrate that the deposited film was HA, the EDX spectra were used to determine the atomic percentages of the major elements, and show that the Ca:P ratio is between 1.65 and 1.77, the ratio found in human bone and therefore the ratio expected for apatite mineral [27, 49]. Figure 4.4 presents two EDX spectra for hydroxyapatite layers on a macroporous film, of which the SEM image is shown in Figure 4.4a. Figure 4.4b displays several peaks due to elements in the specific area probed, notable peaks labeled on the spectra are Si at 1.7 keV, Cl at 2.6 keV, and Ca and 3.7 keV. The Ca:P ratio was determined to be 1.7, which falls in the accepted range, suggesting that an apatite mineral has been deposited. In comparison, Figure 4.4c is an EDX spectrum collected on an area where the silicon sub-layer is exposed, with a prominent peak due to silicon and essentially no other peaks. A similar argument as above can be made for EDX spectra collected on another area of the sample presented in Figure 4.5 with Ca:P falling with in the accepted range for apatite deposits with the exception of Figure 4.5d which yielded a much higher ratio. Other elements found in the EDX spectrum shown in Figures 4.4 and 4.5 include K, Mg, and S. These elements are known to be important in biological mineralization and therefore are expected to be present in minor concentrations [44, 48]. Traces of

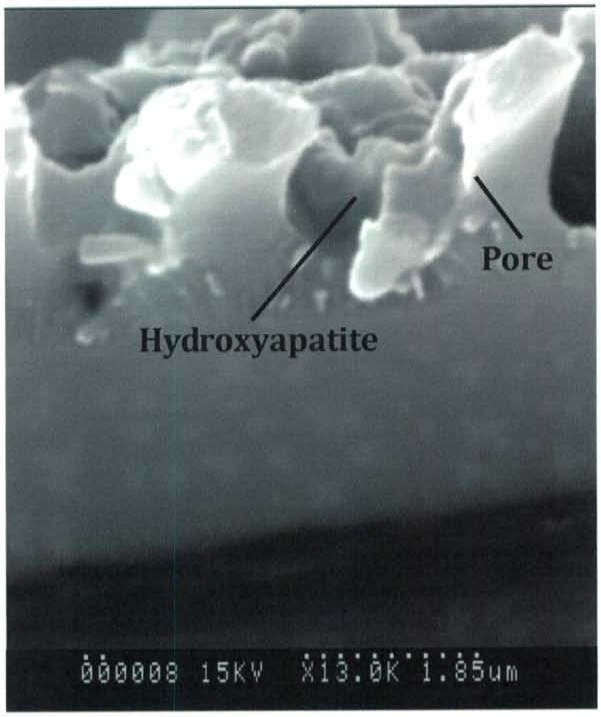

(a)

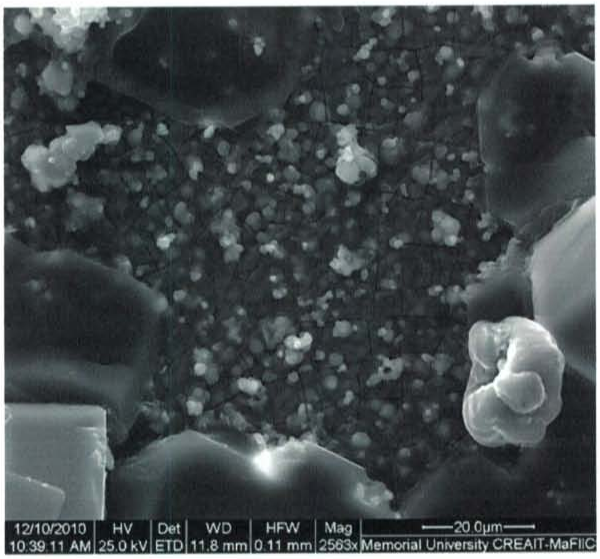

(b)

Figure 4.3: a) Cross sectional SEM of macroporous silicon with hydroxyapatite visible in the pores. b) SEM image of hydroxyapatite on macroporous silicon.

these elements have been reported in other studies of EDX spectrum collected in HA deposition experiments previously [2, 27, 44, 48, 53, 54, 89].

The deposition of the bone mineral hydroxyapatite, $Ca_{10}(PO_4)_6(OH)_2$, on porous silicon has been shown using several methods from passive deposition [49], electrochemical deposition [53], laser-liquid-solid interaction [48], and high frequency arc ablation [51, 52] to name a few. In Ref. [48], laser-liquid-solid (LLSI) interaction was reported to promote and enhance the HA nucleation process resulting in similar distributions when compared to simple immersion in SBF. Pastor *et al.* studied the deposition of hydroxyapatite on electrochemically oxidized mesoporous silicon films by passive deposition and cathodic bias interaction to promote HA precipitations on the silicon surface [49]. It was found that the negative polarization of the porous silicon sample provoked the degradation of the porous structure. Simultaneously, HA precipitates were noted at the sites of hydrogen gas evolution. The cathodic bias of the silicon then promotes bioactivity on the surface [49].

Further, the macroporous samples immersed in SBF were studied using EDX elemental mapping to determine the overall distribution of the deposited elements. Figure 4.6 is a selection of the images collected from the elemental surface scan for a macroporous sample with HA deposits on the surface. Figures 4.6a and 4.6b show the areas containing oxygen and silicon, respectively. Figures 4.6c and 4.6d show the distribution of calcium and phosphate on the sample. Comparison of the EDX elemental maps with the plan view SEM image (Figure 4.6e) shows a distribution of

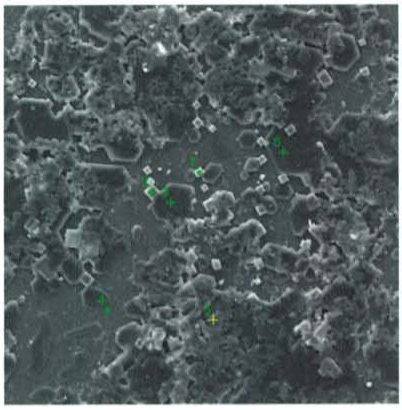

(a)

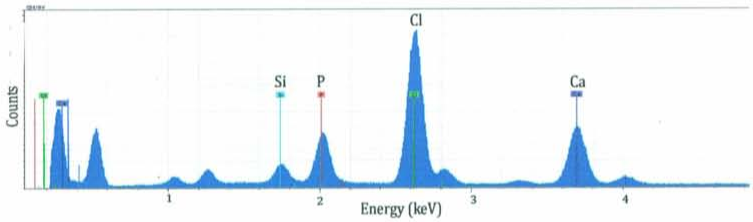

(b)

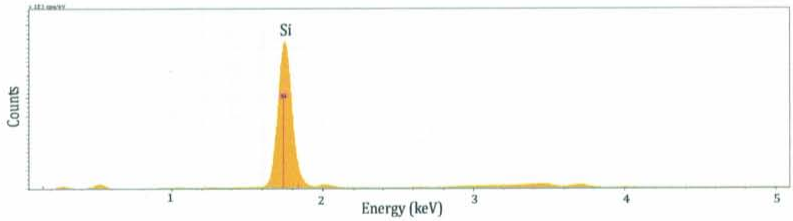

(c)

Figure 4.4: EDX spectra from macroporous sample with pores filled with hydroxyapatite. a) SEM of the probed area, b) and c) EDX spectra.

(a)

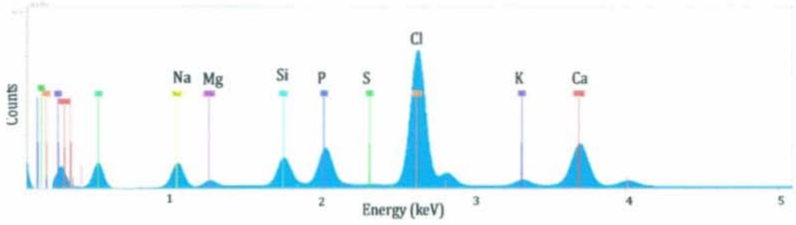

(b)

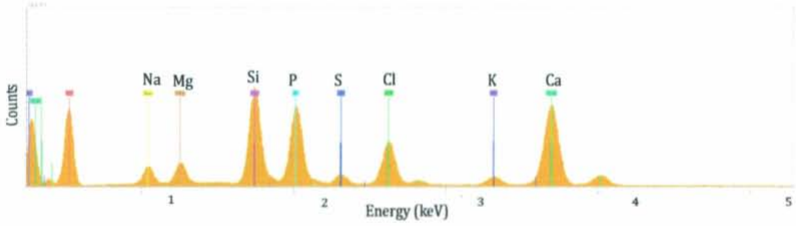

(c)

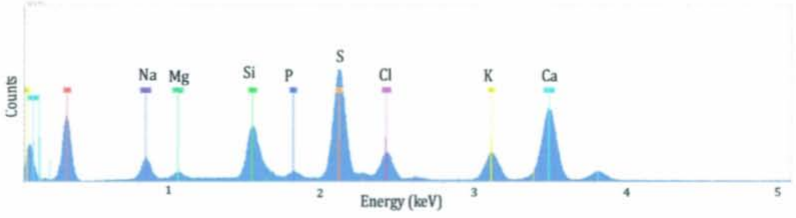

(d)

Figure 4.5: EDX spectra from macroporous sample with pores filled with hydroxyapatite. a) SEM of the area, b), c), and d) EDX spectra

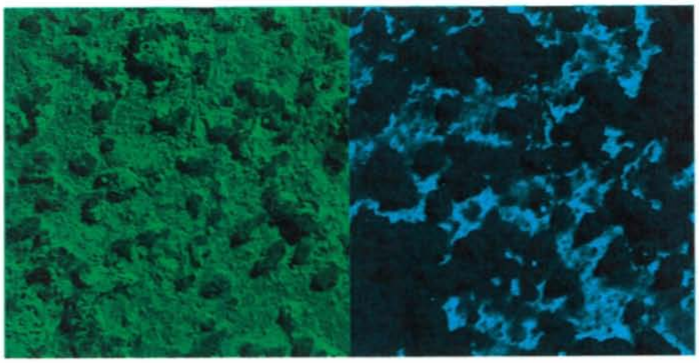

(a) Oxygen (b) Silicon

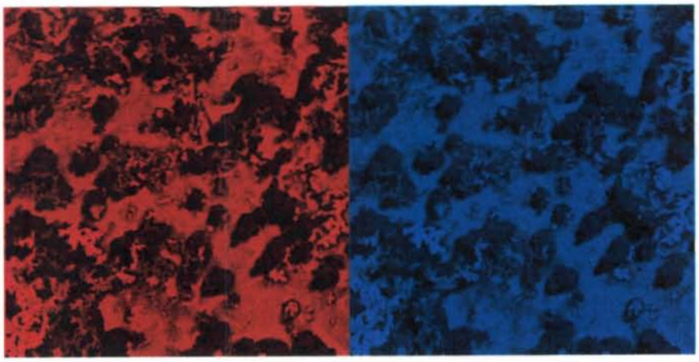

(c) Calcium (d) Phosphate

(e) Original

Figure 4.6: Results from Elemental Map. EDX peaks - Si: 1.7 keV, Cl: 2.6 keV, Ca: 3.7 keV.

Si in the areas where no deposit is present. O is present in all areas, which is also expected due to its prescence on the silicon surface as an oxide and in the HA. The distribution of both Ca and P notably occur in the same areas. For $Ca_{10}(PO_4)_6(OH)_2$ deposits this is expected.

Finally, to demonstrate the distribution of the HA across a portion of the sample, an elemental linescan, shown in Figure 4.7, was done. The areas where deposits are obvious show the elements Ca and P, or Na and Cl depending on the area.

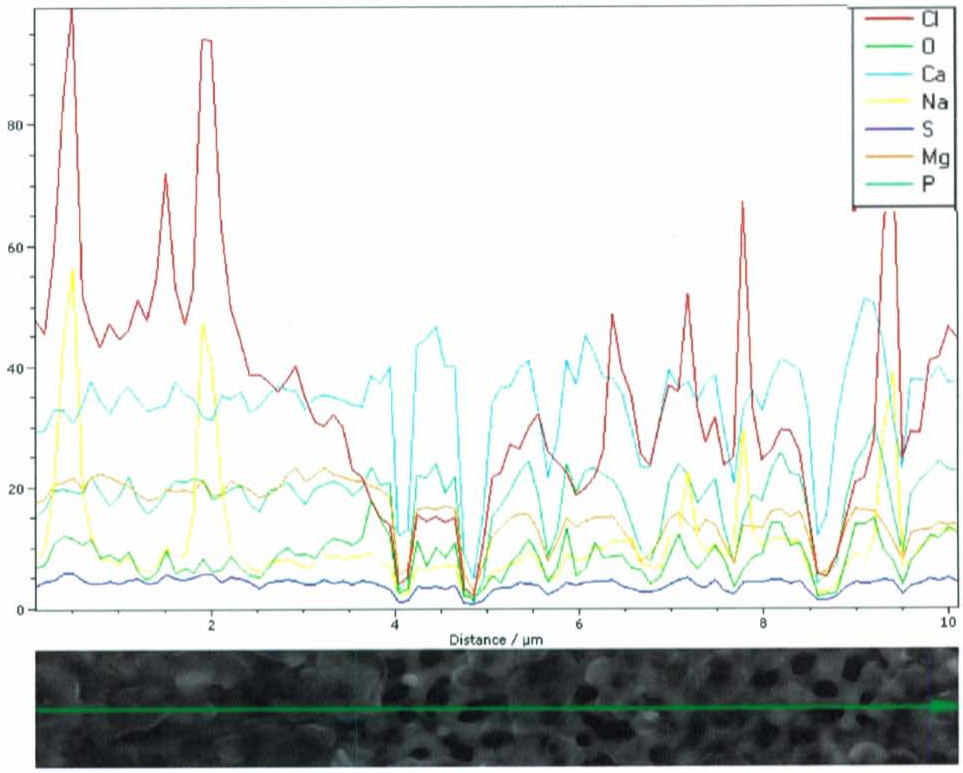

Figure 4.7: EDX linescan across silicon - HA layer.

Chapter 5

Conclusions

Porous silicon films were formed by anodic etching techniques resulting in p^- type microporous silicon films with porosity range of 59% - 85% and n^+ type samples with porosities 25% - 50%. For p^- films the porosities were determined using an optical reflectance method and found to be independent of applied current and dependent on HF concentration in electrolyte. To form samples of this porosity range on p^- type bulk, HF concentrations between 19.6% and 44.1% were employed. For n^+ type samples, the porosities were determined gravimetrically and compared with the previously mentioned optical method allowing the conclusion that the optical method was not valid due to optical anisotropy resulting from a columnar pore morphology.

The fabrication of macroporous silicon films in an organic electrolyte containing acetonitrile, formed on p^- type bulk silicon, was confirmed using scanning electron microscopy. This initial report shows a dependence of the resulting pore diameter,

d_{pore}, on the applied current. An estimate of the pore diameter can be found using $d_{pore} = 0.13 \cdot j + 0.46$ where j is the current density.

Characterization of micro- and mesoporous silicon films by Brillouin light scattering spectroscopy revealed peaks due to the Rayleigh surface mode and two bulk acoustic modes; a transverse mode and a longitudinal mode. It is shown that increasing porosity results in decreasing phonon velocity as expected based on results reported for films fabricated on bulk silicon with resistivity other than those used in this work. Fitting of the experimentally determined velocities for the p^- type samples to $v = v_o(1-\xi)^m$ revealed information about the microstructural details of the porous layer. It was shown that the samples have a ordered, and less open pore structure, agreeing with the expected structure of the material.

The phonon velocities were used to calculate the elastic constants, Young's modulus, and the bulk modulus for each film. The elastic constants showed excellent agreement with values reported for microporous silicon of different bulk resistivity, and were shown to be much smaller than values reported for p^+ type mesoporous samples with cubic symmetry. Values of Young's modulus over the wide range of porosity presented in this work were fit to a model for open celled foams. The results are much different than previously reported for p^+ type samples which can be attributed to differences in pore morphology for microporous silicon and mesoporous silicon.

The dissolution of micro, meso, and macroporous silicon films in simulated body

fluid demonstrated a dependence on the specific surface area of the sample, with those films with a large surface area samples having the fastest dissolution rates. Macroporous silicon samples showed similar dissolution rates to those of the controls due to the low specific surface area. Adapting a relation for the etch rate of porous silicon in HF, an equation for which dissolution of the films based on the samples surface area was demonstrated. Knowledge of the rate of breakdown of the porous film in SBF is required to properly understand the breakdown of the porous film *in vivo*. Further, these results will allow fabrication of custom porous silicon films with a pre-determined dissolution rate.

The bioactivity of macroporous films is demonstrated through the deposition of hydroxyapatite on its surface. EDX and SEM studies are reported to show the deposition of this mineral on the surface of the π-Si, agreeing with previously reported results.

The demonstrated bioactivity, and controllable porosity and elastic moduli allows for the use of porous silicon as tunable biomaterial in a wide range of applications. Fabrication and characterization of porous silicon films on p^- type bulk silicon at intermediate HF concentrations in electrolyte then reported here are required, but expected to result in excellent control of the resultant porosity and elastic properties. Moreover, work on the deposition of HA on these tunable microporous silicon films with large surface areas requires more work. It is documented that HA deposits at sites of dissolution for methods involving cathodic bias. Using the dissolution data

presented in this work, it is speculated that by controlling the dissolution of the porous layer, hydroxyapatite deposition in SBF could be accelerated and optimized.

Bibliography

[1] Lanza, R. P., Langer, R., and Vacanti, J. *Principles of Tissue Engineering.* Academic Press, New York, (2000).

[2] Coffer, J. L., Whitehead, M. A., Nagesha, D. K., Mukherjee, P., Akkaraju, G., Totolici, M., Saffie, R. S., and Canham, L. T. *Phys. Stat. Sol. a* **202**, 1451 (2005).

[3] Chin, V., Collins, B. E., Sailor, M. J., and Bhatia, S. N. *Adv. Mater.* **13**, 1877 (2001).

[4] Canham, L. T., Reeves, C. L., King, D. O., Branfield, P. J., Crabb, J. G., and Ward, M. C. L. *Adv, Mater.* **8**, 850 (1996).

[5] Oisten, M. K. and Bergstrom, P. L. *Phys. Stat. Sol. A* **206**, 1278 (2009).

[6] Duttagupta, S. P., Chen, X. L., Jenekhe, S. A., and Fauchet, P. M. *Sol. Stat. Commun.* **101**, 33 (1997).

[7] Halimaoui, A. *in Properties of Porous Silicon (L. Canham)*, chapter 1, 12. Inst. of Eng. Tech. (1997).

[8] Lehmann, V. *Electrochemistry of Silicon.* (Wiley-VCH, 2002).

[9] Uhlir, A. *Bell Systems Tech. J.* **35** (1956).

[10] Theunissen, M. J. J. *J. Electrochem Soc.* **119**, 351 (1972).

[11] Canham, L. T. *Appl. Phys. Lett* **57**, 1046 (1990).

[12] Bisi, O., Ossicini, S., and Pavesi, L. *Surf. Sci. Rep.* **38**, 1 (2000).

[13] Ilyas, S. and Gal, M. *IEEE Xplor.* **1** (2006).

[14] Polomska, A. M. and Andrews, G. T. *Phys. Stat. Sol. c* **6**, 1665 (2009).

[15] Andrews, G. T., Polomska, A. M., Vazsonyi, E., and Volk, J. *Phys. Stat. Sol. a* **204**, 1372 (2007).

[16] Parsons, L. C. and Andrews, G. T. *App. Phys. Lett.* **95**, 241909 (2009).

[17] Ilyas, S. and Gal, M. *IEEE* , 427 (2006).

[18] Peckham, J. B.sc. (honours), Memorial University of Newfoundland, (2009).

[19] Foll, H., Christopersen, M., Cartensen, J., and Hasse, G. *Mater. Sci. Eng.* **39**, 93 (2002).

[20] Canham, L. T. *in Properties of Porous Silicon (L. Canham)*, chapter 2, 83. Inst. of Eng. Tech. (1997).

[21] Herino, R. *in Properties of Porous Silicon (L. Canham)*, chapter 2, 89. Inst. of Eng. Tech. (1997).

[22] Bomchil, G., Herino, R., Barla, K., and Pfister, J. C. *J. Electrochm. Soc.* **130**, 1611 (1983).

[23] Fan, H. J., Kuok, M. H., Boukherroub, R., Baribeau, J. M., Fraser, J. W., and Lockwood, D. J. *Phys. Rev. B.* , 65 (2002).

[24] Propst, E. K. and Kohl, P. A. *J. Electrochem. Soc.* **141**, 1006 (1994).

[25] Levy-Clement, C., Lust, S., Bastide, S., Le, Q. N., and Sarti, D. *Phys. Stat. Sol.* **197**, 27 (2003).

[26] Ponomarev, E. A. and Levy-Clement, C. *Electrochem. Solid-State Lett.* **1**, 42 (1998).

[27] Sun, W., Puzas, J. E., Sheu, T. J., and Fauchet, P. M. *Phys. Stat. Sol.* **204**, 1429 (2007).

[28] Barla, K., herino, R., Bomchil, G., Pfister, J. C., and Freund, A. *J. Cryst. Growth* **68**, 727 (1984).

[29] Populaire, C., Remaki, B., Lysenko, V., Barbier, D., Artmann, H., and Pannek, T. *App. Phys. Lett.* **83**, 1370 (2003).

[30] daFonseca, R. J. M., Saurel, J. M., Foucaran, A., Camassel, J., Massone, E., and Taliercio, T. *J. Mat. Sci.* **30**, 35 (1995).

[31] Bellet, D., Lamagnere, P., Vincent, A., and Brechet, Y. *J. Appl. Phys.* **80**, 3772 (1996).

[32] Fang, Z. Q., Hu, M., Zhang, W., and Yang, H. *Thin Solid Films* **517**, 2930 (2009).

[33] Beghi, M. G., Bottani, C. E., Ghislotti, G., Amato, G., and Boarino, L. *Thin Solid Films* **297**, 110 (1997).

[34] Lockwood, D. J., Kuok, M. H., Ng, S. C., and Rang, Z. L. *Phys. Rev. B* **60**, 8878 (1999).

[35] Fan, H. J., Kuok, M. H., Ng, S. C., Lim, H. S., Liu, N. N., Boukherroub, R., and Lockwood, D. J. *J. Appl. Phys.* **94**, 1243 (2003).

[36] Andrews, G. T., Zuk, J., Kiefte, H., Clouter, M. J., and Nossarzewska-Orlowska, E. *Appl. Phys. Lett.* **69**, 1217 (1996).

[37] Andrews, G. T., Clouter, M. J., and Zuk, J. *Semicond. Sci. and Tech.* **19**, 1306 (2004).

[38] Andrews, G. T., Polomska, A. M., Vazsonyi, E., and Volk, J. *Phys. Stat. Sol.* **204**, 1372 (2007).

[39] Canham, L. T. *Adv. Mater.* **7**, 1033 (1995).

[40] Canham, L. T., Reeves, C. L., Loni, A., Houlton, M. R., Newey, J. P., Simons, A. J., and Cox, T. I. *Thin Solid Films* **297**, 304 (1997).

[41] Rosengren, A., Wallman, L., Bengtsson, M., Laurell, T., Danielsen, N., and Bjursten, L. M. *Phys. Stat. Sol. a* **182**, 527 (2000).

[42] Oyane, A., Kim, H. M., Furuya, T., Kokubo, T., Miyazaki, T., and Nakamura, T. *J. Biomed. Mater. Res. A* , 188 (2003).

[43] Hench, L. L. *J. Am. Ceram. Soc.* **74**, 1487 (1991).

[44] Kokubo, T., Kim, H. M., and Kawashita, M. *Biomater.* **24**, 2161 (2003).

[45] Anderson, S. H. C., Elliott, H., Wallis, D. J., Canham, L. T., and Powell, J. J. *Phys. Stat. Sol.* **197**, 331 (2003).

[46] Poondi, D., Subramanium, R., Otooni, M., and Singh, J. *J. Mater. Synth. and Proc.* **6**, 89 (1998).

[47] Poondi, D., Dobbins, T., and Singh, J. *J. Mater. Sci.* **35**, 6237 (2000).

[48] Pramatarova, L., Pecheva, E., Dimova-Malinovska, D., Pramatarova, R., Bismayer, U., Petrov, T., and Minkovski, N. *Vacuum* **76**, 135 (2004).

[49] Pastor, E., Matveeva, E., Parkhutik, V., Curiel-Esparza, J., and Millan, M. C. *Phys. Stat. Sol.* **4**, 2136 (2007).

[50] Li, W., Coffer, J. L., Chen, Y., Pinizzotto, R. F., Newey, J., and Canham, L. T. *J. Am. Chem. Soc.* **120**, 11706 (1998).

[51] Coffer, J. L., Montcamp, J.-L., Aimone, J. B., and Weis, R. P. *Phys. Stat. Sol. a* **197**, 336 (2003).

[52] Weis, R. P., Chen, Y., and Coffer, J. L. *Electrochem . Solid State Lett.* **5**, C22 (2002).

[53] Pastor, E., , Salonen, J., Lehto, V. P., and Matveeva, E. *Phys. Stat. Sol. A* **206**, 1333 (2009).

[54] Sun, W., Puzas, J. E., Sheu, T. J., Liu, X., and Fauchet, P. M. *Adv. Mater.* **19**, 921 (2007).

[55] Peckham, J. and Andrews, G. T. *Submitted to Thin Solid Films* (2011).

[56] Parsons, L. C. Bachelor of science thesis, Memorial University of Newfoundland, (2006).

[57] Bellet, D. *Inst. Eng. Tech.* **38**, 38 (1997).

[58] Theiss, W. *Surf. Sci. Rep.* **29**, 91 (1997).

[59] Lehmann, V. and Ronnebeck, S. *J Electrochem. Soc.* **146**, 2968 (1999).

[60] Lust, S. and Levy-Clement, C. *Phys. Stat. Sol. (a)* **182**, 17 (2000).

[61] Ponomarev, E. A. and Levy-Clement, C. *J. Porous Mater.* **7**, 51 (2000).

[62] Lust, S. and Levy-Clement, C. *J. Electrochem. Soc.* **149**, C338 (2002).

[63] Young, C. K. Bachelor of science thesis, Memorial University of Newfoundland, (2004).

[64] Polomska, A. M. PhD thesis, Memorial Universtiy of Newfoundland, Sept (2009).

[65] Ashcroft, N. W. and Mermin, N. D. *Solid State Physics.* Thomson Learning, 1976.

[66] Hayes, W. and Loudon, R. *Scattering of Light by Crystals.* Dover Publications, 2004.

[67] Sandercock, J. R. *Sol. Stat. Commun.* **26**, 547 (1978).

[68] Young, C. K. Master's thesis, Memorial University of Newfoundland, ((2007)).

[69] Dieulesaint, E. and Royer, D. *Elastic Waves in Solids: Applications to Signal Processing.* J. Wiley, (1980).

[70] Kittel, C. *Introduction to Solid State Physics.* John Wiley and Sons, Inc, 7 edition, (1996).

[71] Birss, R. R. *Symmetry and Magnetism.* North-Holland Publishing Company, (1966).

[72] Kittel, C. *Introduction to Solid State Physics.* John Wiley and Sons, Inc, 8th edition, (2005).

[73] Sandercock, J. R. *J. Phys.* **9**, 566 (1976).

[74] Sandercock, J. R. *Tandem Fabry-Perot Interferometer TFP-1 Operator Manual.* JRS Scientific Instruments, Switzerland, (2001).

[75] Viktorov, I. A. *Rayleigh and Lamb Waves: Theory and Application.* Plenum, New York, (1967).

[76] Munder, H., Berger, M. G., Frohnhoff, S., Thonissen, M., Luth, H., Jeske, M., and Schultze, J. W. *J. Lumin.* **57**, 223 (1993).

[77] Fan, H. J., Kuok, M. H., Ng, S. C., Boukherroub, R., and Lockwood, D. J. *Appl. Phys. Lett.* **79**, 4521 (2001).

[78] Phani, K. K., Niyogi, S. K., Maitra, A. K., and Roychaudhury, M. *J. Mater. Sci.* **21**, 4335 (1986).

[79] Lockwood, D. J., Wang, A., and Bryskiewicz, B. *Sol. St. Commun.* **89**, 587 (1995).

[80] Lockwood, D. J. and Wang, A. *Sol. St. Commun.* **94**, 905 (1994).

[81] Aliev, G. N., Goller, B., Kovalev, D., and Snow, P. A. *Phys. Stat. Sol. c* **6**, 1670 (2009).

[82] Karp, J. M., Dalton, P. D., and Shoichet, M. S. .

[83] Gibson, L. J. *MRS Bulletin* , 270 (2003).

[84] Al-Douri, Y., Ahmed, N. M., Bouarissa, N., and Bouhmadou, A. *Mater. Des* **32**, 4088 (2011).

[85] Gibson, L. J. and Ashby, M. F. *Cellular Solids: Structure and Properties.* Permagon New, York, (1988).

[86] Andrews, G. T. *Elastic and Structural Properties of Supported Porous Silicon Layers.* PhD thesis, Memorial University of Newfoundland, (1999).

[87] Halimaoui, A. *Surf. Sci. Lett.* **306**, L550 (1994).

[88] Herino, R., Bomchil, G., Barla, K., Bertrand, C., and Ginoux, J. L. *J. Electrochem. Soc.* **134**, 1994 (1987).

[89] Whitehead, M. A., Fan, M. S. D., Mukherjee, B. S. P., Akkaraju, G. R., Canham, L. T., and Coffer, J. L. *Tissue Eng.* **14**, 195 (2008).

[90] Pecheva, E., Petrov, T., Lungu, C., Montgomery, P., and Pramatarova, L. *Chem. Eng. Jnl.* **137**, 144 (2008).

[91] Pavesi, L. *Rivista del Nuovo Cimento* **20**, 1 (1997).

[92] Pena, C. and Torres, J. *Surf. Rev. Lett.* **9**, 1821 (2002).

Appendix A

Spectral Reflectance

In this appendix the thickness of the porous silicon samples was determined from the spectral reflectance spectrum and compared to the estimated thickness in an attempt to determine if a porosity gradient exists in the samples. Multiple interference fringes are found in the reflectance spectrum which can be used to determine the optical thickness, d_o, of a given sample assuming that the interface between the porous layer and the substrate is parallel and that the refractive index is a smooth function of the wavelength [91].

A.1 Theory

The reflected light from a film contains both light reflected from the air-porous silicon interface, as well as light transmitted through the porous silicon film and reflected from the porous silicon-bulk silicon interface [92]. This is described by the relation

$$\frac{1}{\lambda_{m+1}} - \frac{1}{\lambda_m} = \frac{1}{2n_{\pi-Si}d}. \tag{A.1}$$

where λ_m and λ_{m+1} are the corresponding wavelengths of adjacent m and $m+1$ reflectance maxima, $n_{\pi-Si}$ is the refractive index of the porous layer and d is layer thickness [91]. This can be re-written using the optical thickness, d_o such that

$$d_o = \frac{1}{2}(\frac{1}{\lambda_{m+1}} - \frac{1}{\lambda_m})^{-1} \tag{A.2}$$

A.2 Experimental Setup

White light from an Ocean Optics LS-1 tungsten halogen light source was coupled into a set of 6 optical fibres of an Ocean Optics QR600-7-UV-125F reflection/backscattering probe with wavelength range of 300 - 1100 nm. The reflected light was returned back through a separate optical fiber in the probe and into an Ocean Optics USB2000 miniature fiber spectrometer. The reflected light was analyzed in the spectrometer and presented in Ocean Optics Spectra Suite software. A broadband mirror was used as to record a reference spectrum for the light source and the halogen light source was blocked to record a dark reference spectra. Both backgrounds were removed from the spectrum before analysis. The wavelengths corresponding to the maxima of the interference fringes were determined by fitting Gaussian peaks to the data using graphical analysis software.

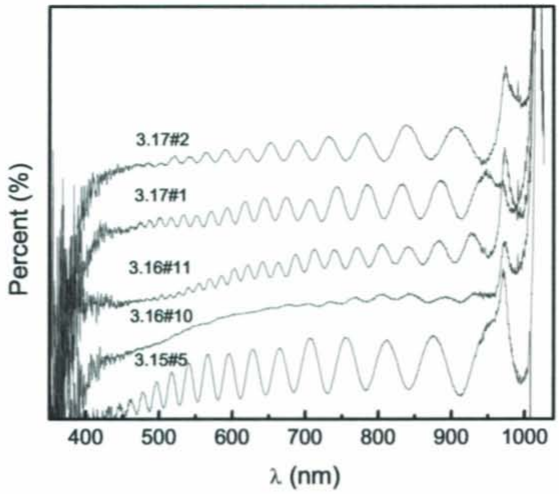

Figure A.1: Reflectance spectra for samples formed in 1.5 49%HF : 1 Ethanol electrolyte.

A.3 Results and Discussion

The spectra collected in this work are presented in Figures A.1 to A.6. The determined optical thickness, d_o, for each sample is given in Table A.1, along with the refractive indices determined optically as described in Chapter 2.

Figure A.8 shows a comparison of the thickness of the sample, determined using the accepted value of n in the backscattering reflectance data ($d_{SR} = d_o n$) versus the estimated sample thickness, d, determined using $d = 1.05t \cdot j^{0.89}$ where j is the current density [8]. The dashed line represents $d_{SR} = d_{est}$.

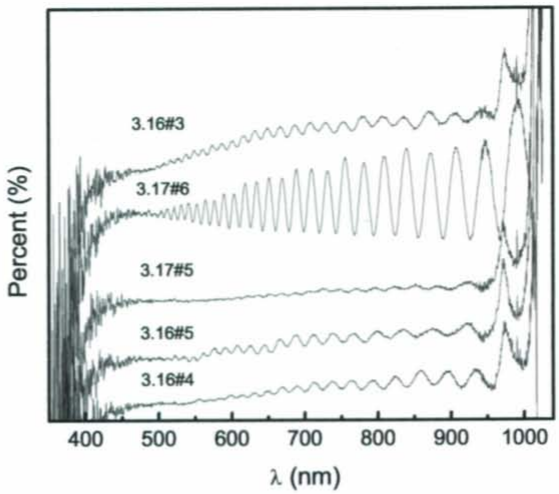

Figure A.2: Reflectance spectra for samples formed in 1 49%HF : 1 Ethanol electrolyte.

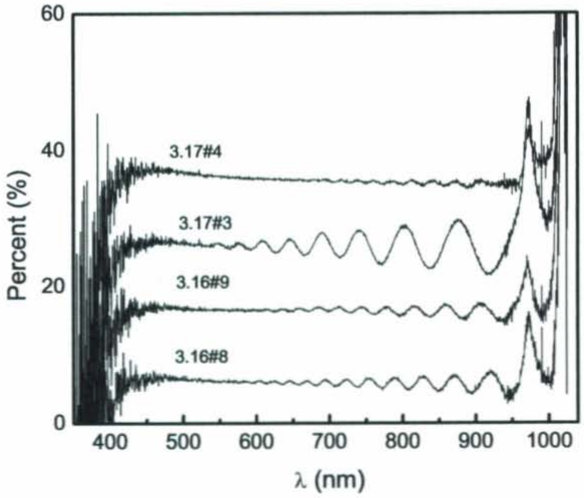

Figure A.3: Reflectance spectrum for samples formed in 1 49%HF : 9 Ethanol electrolyte.

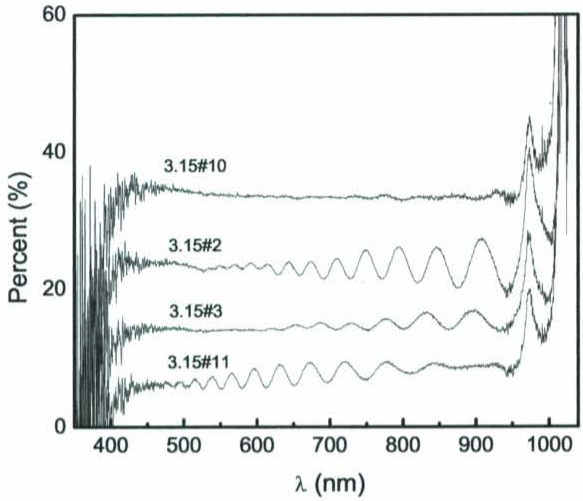

Figure A.4: Reflectance spectra for samples formed in X 49%HF : 1 Ethanol electrolyte.

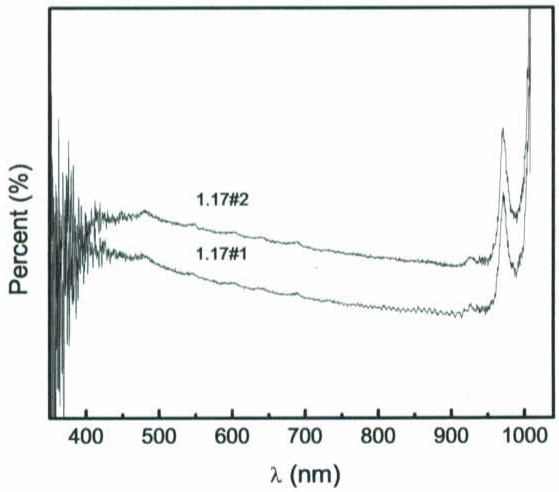

Figure A.5: Reflectance spectra for samples formed on n-type bulk silicon.

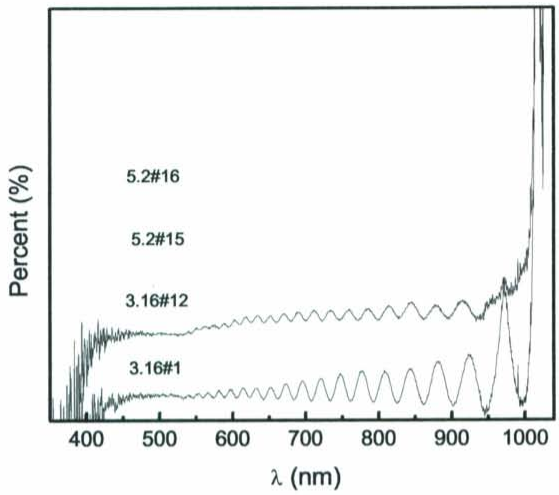

Figure A.6: Reflectance spectra for samples formed on different resistivity p^- type bulk silicon at 28 mA.

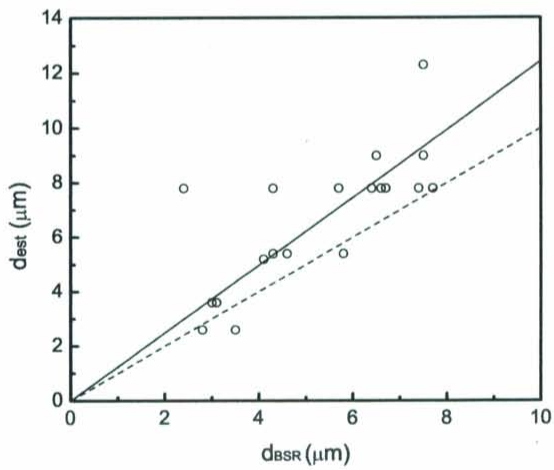

Figure A.7: Comparison of the thickness of samples determined from reflectance data using the accepted n values versus expected thickness estimated using $d = 1.05t \cdot j^{0.89}$ where j is the current density [8]. The dashed line represents $d_{BSR} = d$ and the solid line represents a fit to the data forced through the origin resulting in a slope of 1.24.

Table A.1: Thickness determined through spectral reflectance compared to estimated values.

Sample	d_o (μm)	n ($\pm$ 4%)	d_{SR} (μm)	d_{est} (μm)
3.15#10	7.5	2.10	3.5	2.6
3.16#8	8.7	1.88	4.6	5.4
3.16#9	8.2	1.92	4.3	5.4
3.17#3	4.8	1.98	2.4	7.8
3.17#4	11.7	2.07	5.7	7.8
3.15#2	6.6	2.14	3.1	3.6
3.15#3	5.9	2.00	3.0	3.6
3.15#11	5.1	1.84	2.8	2.6
3.16#1	11.6	1.54	7.5	9.0
3.16#12	10.2	1.58	6.5	9.0
3.16#3	11.5	1.54	7.5	12.3
3.16#4	10.6	1.57	6.7	7.8
3.16#5	9.5	1.48	6.4	7.8
3.17#5	6.6	1.54	4.3	7.8
3.17#6	12.1	1.58	7.7	7.8
3.15#5	5.6	1.35	4.1	5.2
3.16#10	8.4	1.28	6.6	7.8
3.16#11	9.6	1.29	7.4	7.8
3.17#1	7.3	1.25	5.8	5.4
3.17#2	6.0	1.27	4.7	5.4
1.17#1	-	2.92		
1.17#2	-	2.48		
3.15#7 GaIN	14.2	1.37	10.4	6.9
3.15#8 GaIN	7.8	1.48	5.3	3.6

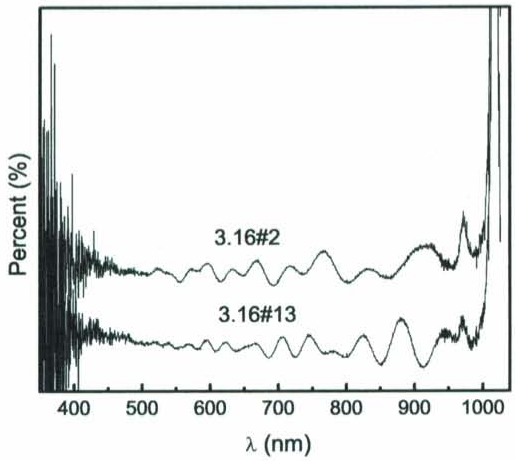

Figure A.8: Reflectance spectra collected for bilayer porous silicon samples. Sample 3.16#2 was fabricated to have a 2 μm think 74% porous layer above a 2 μm thick 63% layer. Sample 3.16#13 contained a 4 μm think 74% porous layer above a 1 μm thick 63% layer.